1

Melt motion in a Czochralski crystal puller with a non-uniform axisymmetric magnetic field: isothermal motion

By L. N. HJELLMING[1], P. A. TOLLEY[1] AND J. S. WALKER[2]

[1] Department of Mechanical Engineering and Engineering Science, University of North Carolina-Charlotte, Charlotte, NC 28223, USA

[2] Department of Mechanical and Industrial Engineering, University of Illinois, Urbana, IL 61801, USA

The use of magnetic fields during the growth of semiconductor crystals from the melt in a Czochralski (CZ) crystal puller has shown promise in controlling the heat and mass transport to the growth interface. The magnetic field suppresses turbulence and thermal convection in the melt in which large thermal gradients are present, thus improving the quality of the crystal. In this paper, analytical solutions are presented for the isothermal melt motion and electric current density driven by the differential rotation of the crystal and crucible about their common vertical axis. There is an applied, non-uniform, axisymmetric magnetic field with only radial and axial components which are independent of the azimuthal coordinate. The melt motion with a uniform axial magnetic field represents a singular limit of the flow considered here: as the radial magnetic field component goes to zero, the radial and axial (meridional) velocity components decrease in magnitude by a factor of M^{-1}, where M is the large Hartmann number. The uniform axial field is a singular limit because the centrifugal acceleration due to the azimuthal velocity is exactly perpendicular to the magnetic field. Since the radial isothermal motion near the growth interface controls the radial distributions of dopants and impurities in the crystals, a non-uniform axisymmetric magnetic field is better than the uniform axial field. In addition, the axisymmetric field avoids the detrimental deviations from axisymmetric heat and mass transport associated with a uniform transverse (horizontal) magnetic field.

Two classes of shaped fields are considered, with only one class leading to the presence of the large meridional flow driven by differential rotation. The small electrical conductivity of the crystal plays an important role in determining the behaviour of the melt's angular velocity, which is constant along each magnetic field line. Results for two simple field configurations are presented in order to illustrate the effect of the field configuration on the nature of the meridional circulation and the potential for flow tailoring with the shaped field.

1. Introduction

In recent years, the improvement of the quality of silicon and gallium-arsenide crystals has been achieved with novel growth methods and through the use of sophisticated control systems during crystal growth. These developments reflect the increasing demand of the electronics industry for high-quality, large-diameter semiconductor crystals. The Czochralski (CZ), liquid-encapsulated Czochralski,

horizontal and vertical Bridgman, and float-zone systems involve growth from a melt with large thermal gradients. Unsteady or non-uniform heat and mass transfer to the growth interface may produce high dislocation and defect densities, growth striations, and non-uniform dopant and impurity distributions, all of which are unfavourable properties in the final crystal.

In traditional CZ crystal growth, which is the method of choice for large-diameter silicon crystals, the high thermal gradients in the melt produce significant buoyant convection, and the flow is turbulent. The crystal is rotated about its vertical axis in order to produce a viscous shear layer isolating the growth interface from the flow irregularities in the bulk of the melt. The crucible is also rotated to minimize the effects of any slight deviations from axisymmetry in the heaters (see figure 1 a). The silicon melt is contained in a quartz (SiO_2) crucible which continuously erodes with contact to the melt, releasing oxygen and other impurities into the melt. While almost all of the oxygen evaporates from the free surface, the portion that remains in the melt is transported to the growth interface, and the oxygen and impurity distributions in the crystal may be non-uniform and undesirably high. The fluctuations in heat transfer at the growth interface cause the crystal to melt and re-solidify, producing defects and random growth striations which contribute to the micro- and macro-scale non-uniformity of the crystal (Kuroda, Kozuka & Takano 1984).

The use of magnetic fields to control the flow field, heat transfer and mass transfer during the growth of large-diameter semiconductor crystals has received considerable attention in the last ten years (see e.g. Langlois, Kim & Walker 1992). Owing to the large electrical conductivity of semiconductor melts, the application of a magnetic field suppresses flow across magnetic field lines, and hence alters the entire melt motion, through the presence of the electromagnetic Lorentz force. Recently, detailed theoretical and experimental work has clarified the nature of the transport processes in CZ growth systems when a magnetic field is applied (see e.g. Hirata & Hoshikawa 1989; Hjellming 1990; Ravishankar, Braggins & Thomas 1990; Thomas *et al.* 1990; Williams, Walker & Langlois 1990). Originally it was thought that with the suppression of the melt motion by the magnetic field, the heat and mass transfer would be such as to produce better crystals. It has since been shown that the magnetic field introduces a degree of complexity and sensitivity to the interactions between the flow field and transport processes not present in the traditional non-magnetic CZ growth systems, and that the effects of a magnetic field are not always positive.

To date, most of the theoretical work on the transport processes in magnetic CZ silicon growth systems has concentrated on the application of a uniform magnetic field aligned with the crystal growth axis, called an axial or vertical magnetic field. The axisymmetry of this field is appealing, but both experimental and theoretical results have shown that this field configuration has serious disadvantages (Hjellming 1990; Ravishankar *et al.* 1990). With the axial field, the centrifugal pumping flow driven by differential rotation of the crystal and crucible is highly suppressed and varies as B_0^{-3}, where B_0 is the magnetic flux density (Hjellming & Walker 1986). The centrifugal pumping flow provides the radial convective mass transport at the growth interface needed to sweep away rejected dopants and impurities. The large suppression of this flow with an axial magnetic field leads to extremely large non-uniform radial distributions of dopants and impurities (Ravishankar *et al.* 1990).

The thermally driven flows due to buoyancy and the variation of surface tension with temperature also affect the mass transport in several ways when an axial field
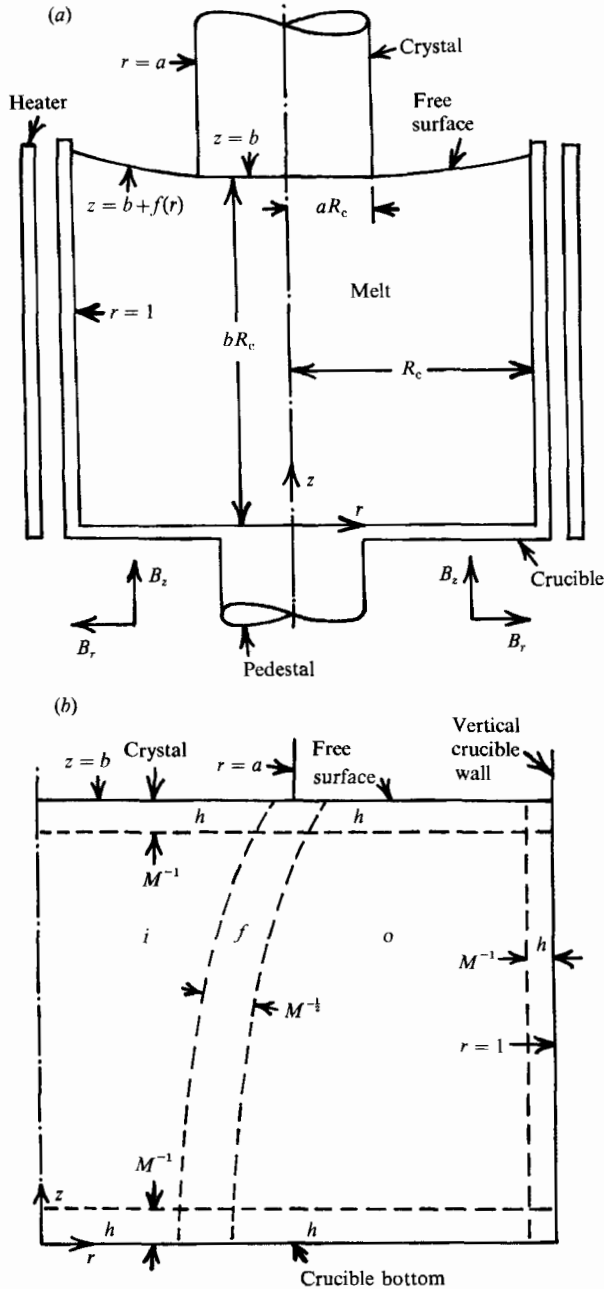
FIGURE 1. (a) Model Czochralski crystal growth system with a non-uniform, axisymmetric magnetic field $\boldsymbol{B} = B_r \boldsymbol{r} + B_z \boldsymbol{z}$. The cylindrical coordinates are normalized by the inside crucible radius. (b) Meridional section showing subregions of the melt for $M \gg 1$.

is applied. First, the magnitude of the thermally driven flow circulation varies as B_0^{-2} and depends strongly on depth, so that the relative contributions of convection and conduction to the total heat transfer change with depth and magnetic field strength. During the initial stages of growth with a field strength of 0.2 T, convective heat transfer dominates. As growth continues and the melt volume is depleted, the thermally driven flows decrease in magnitude, and conduction becomes the dominant

heat transfer mechanism for $B = 0.2$ T (Hjellming 1990). For a stronger magnetic field, the shift from convection- to conduction-dominated heat transfer occurs at a larger depth, i.e. at an earlier stage of growth. For extremely strong magnetic fields, conduction dominates from the beginning of crystal growth. For conventional CZ crystal growth, convective heat transfer dominates at all stages (Langlois 1984), and the heat input from the radiant heaters needed to sustain stable growth is low. As conduction becomes the primary heat transfer mechanism for magnetic CZ growth, the heat input needed for stable growth increases, resulting in higher temperatures on the vertical crucible wall (Hjellming 1990). Since the ablation or erosion of the crucible increases with increasing temperature, the increased oxygen levels in crystals grown in an axial field are due in part to the increased ablation of the crucible (Ravishankar *et al.* 1990).

A second effect of the magnetic field on mass transfer is that turbulent mixing of impurities and dopants is eliminated. For species with low diffusion coefficients such as oxygen ($D \sim 10^{-8}$ m^2/s), the convective mass transfer, provided by the thermally driven flows, is the dominant mechanism for mixing in the melt. At large depths and low field strengths, it is possible that the oxygen distribution may reach a well-mixed steady state in the melt. However, as the depth decreases or the field strength increases, the thermally driven flow circulation decreases, and a well-mixed steady-state concentration is not achieved. Furthermore, as the melt depth decreases, the thermally driven flow ceases to provide a circulation of oxygen-rich fluid toward the free surface, where oxygen evaporates, but actually provides a direct circulation from the crucible to the growth interface (Hjellming & Walker 1988*b*). Since the centrifugal pumping flows are more strongly suppressed by an axial field than are the thermally driven flows, and also circulation decrease with depth, the former cease to provide a vigorous circulation for increased mixing of the dopants and impurities in the melt region near the growth interface as the depth decreases or the field strength increases.

Some of the detrimental characteristics of the axial field can be eliminated with a uniform transverse or horizontal magnetic field. With the field oriented parallel to the growth interface, any vertical melt motion is strongly suppressed. A transverse field does not suppress the radial centrifugal pumping near the crystal face which produces more uniform radial concentration distributions, nor does this field suppress the flow driven by the surface tension variation, which draws fluid to the free surface where it can lose oxygen through evaporation. Thus this type of field configuration shows promise in decreasing the oxygen concentration, and improving the radial uniformity. The radial uniformity of oxygen is not significantly affected by changes in the field strength, although it is improved with increased crystal rotation rates (Ravishankar *et al.* 1990), and the radial uniformity is better than that for the axial field or that for conventional CZ crystal growth.

The biggest problem for a transverse field is the enhancement of asymmetries in the thermal and flow fields for certain ranges of magnetic field strength (Williams 1989). A transverse field produces a non-axisymmetric flow. For example, buoyant convection with a strong transverse field consists of a downward flow near the vertical plane composed of the crucible diameters which are parallel to the magnetic field, and an upward flow on both sides of this plane. As long as convection makes a significant contribution to the heat transfer, the temperature field is non-axisymmetric. This means that a point on the rotating crystal face experiences fluctuations in heat flux at twice the frequency of crystal rotation. One purpose of applying a magnetic field is to eliminate such fluctuations in the heat flux at the

growth interface. A transverse magnetic field will also make the mass transport non-axisymmetric. Therefore, the azimuthally averaged concentrations of oxygen and dopants may be relatively uniform in the radial and axial directions, but the azimuthal variations remain (Williams *et al.* 1990; Williams 1989).

An alternative to the uniform unidirectional axial or transverse magnetic field is a non-uniform axisymmetric or shaped magnetic field, which combines the axisymmetry of the axial field and the radial field component needed to suppress vertical melt motion. Hirata & Hoshikawa (1990) have reported significant improvements in the quality of large-diameter silicon crystals grown with an applied 'cusp' magnetic field. This field configuration is easily produced by two solenoidal coils surrounding the crucible and crystal, with the fields of the two coils oriented in opposite directions. As the crystal grows and the melt is depleted, the field configuration may be changed to counteract the effects of a flow field and transport processes which are depth or time dependent.

One of the attractive features of the shaped field is that the flow field can be tailored by the field–melt interaction, such that the heat and mass transfer are optimized for the growth of high-quality crystals. For example, large radial components of the field can be positioned at the free surface and vertical wall regions, where suppression of vertical motion is indicated, but increased radial heat and mass transport are beneficial. Additionally, a significant radial field component with a reduced axial component at the growth interface will enhance radial convective mass transfer. Hicks, Organ & Riley (1989) show that the oxygen distribution in the crystal is more uniform with a non-uniform axisymmetric magnetic field than with an axial field. Hicks & Riley (1989) have theoretically treated the isothermal crystal face boundary layer for both a uniform axial magnetic field and a uniform radial field. These results indicate that the magnetic field orientation has a strong influence on the mass transport at the growth interface.

This paper presents analytical solutions, determined by matched asymptotic expansions, for the flow field due to differential crystal/crucible rotation for an isothermal silicon melt with a general non-uniform axisymmetric magnetic field. The methodology follows that of Hjellming & Walker (1986, hereinafter referred to as HWI). In §2, the problem is formulated for the general field. Section 3 contains the solutions for the azimuthal velocity, electric potential and meridional electric current density, with §4 containing the solutions for the meridional circulations. In §5, two simple non-uniform axisymmetric field configurations are used to illustrate the characteristics of the meridional circulations, with the discussion following in §6.

2. Problem formulation

We consider the model CZ crystal growth system shown in figure 1(*a*), with (r, θ, z) as the cylindrical coordinates. The melt is silicon, with the physical properties listed in table 1. The system is considered to be axisymmetric so that there is no dependence on the azimuthal coordinate, θ, in the dependent variables or boundary conditions. Our first parametric assumption is that the magnetic Reynolds number, $R_m = \mu_m \sigma \Omega R_c^2 \ll 1$, so that the magnetic field produced by any electric currents in the melt or crystal can be ignored. Here, μ_m and σ are the magnetic permeability and electrical conductivity of the melt, while Ω and R_c are the angular velocity and inside radius of the crucible, respectively. The general form of a non-uniform axisymmetric field is

$$\boldsymbol{B} = B_r(r,z)\,\hat{\boldsymbol{r}} + B_z(r,z)\,\hat{\boldsymbol{z}}, \tag{1}$$

(a)	
Density, ρ_0	2330 kg/m³
Kinematic viscosity, ν	3×10^{-7} m²/s
Electrical conductivity, σ	10^6 mho/m
Magnetic permeability, μ_m	$4\pi \times 10^{-7}$ H/m
Electric conductivity of crystal, $\delta\sigma$	3.16×10^4 mho/m
(b)	
Inside crucible radius, R_c	0.095 m
Crystal radius, aR_c	0.038 m
Melt depth, bR_c	0.095 m

TABLE 1. (a) Physical constants of silicon melt; (b) geometry of model Czochralski system.

where r and z are unit vectors, while $\boldsymbol{B}$ satisfies the equations

$$\nabla \cdot \boldsymbol{B} = 0 \tag{2}$$

and

$$\nabla \times \boldsymbol{B} = 0. \tag{3}$$

We confine the analysis to magnetic fields with field strengths of magnitude $|\boldsymbol{B}| \geqslant 0.2$ T throughout the melt. Hjellming & Walker (1988a) show that, for magnetic field strengths greater than 0.2 T, the inertial acceleration terms are negligible, except for the centrifugal acceleration term. With the inertialess approximation, the Navier–Stokes equations are linear in the meridional velocities u_r and u_z, and the flow fields due to differential rotation, buoyancy, thermocapillarity and crystal growth may be found separately. Here, we consider only the centrifugal pumping flow driven by differential rotation of the crystal and crucible, when the melt is treated as isothermal and there is no 'suction' at the crystal face. For a uniform axial field, the meridional flow driven by differential rotation is small, and does not contribute to the convective heat transfer in the melt (Hjellming & Walker 1987). For the shaped field, the meridional flow driven by differential rotation is as large as the thermally driven flows, so that the centrifugal pumping flow must be included in the heat transfer analysis. However, the thermally driven flows are coupled to the rotationally driven flows through the temperature only, with the momentum transport remaining linear in the velocities.

We follow the scalings of HWI for the isothermal melt problem, with the non-dimensional variables denoted by asterisks, where

$$r = R_c r^*, \quad z = R_c z^*; \tag{4a, b}$$

$$u_r = U_c u_r^*, \quad u_z = U_c u_z^*, \quad u_\theta = \Omega R_c u_\theta^*; \tag{5a-c}$$

$$j_r = \sigma \Omega R_c B_0 j_r^*, \quad j_z = \sigma \Omega R_c B_0 j_z^*, \quad j_\theta = \sigma U_c B_0 j_\theta^*; \tag{6a-c}$$

$$F = \Omega R_c^2 B_0 F^*, \quad p = \rho_0 g R_c (b - z^*) + \rho_0 \Omega^2 R_c^2 p^*; \tag{7a, b}$$

$$\boldsymbol{B} = B_0 \boldsymbol{B}^* = B_0 (B_r^* \hat{\boldsymbol{r}} + B_z^* \hat{\boldsymbol{z}}); \tag{8}$$

where

$$U_c = \rho_0 \Omega^2 R_c / (\sigma B_0^2). \tag{9}$$

The physical properties and their symbols are listed in table 1. Here, b is the non-dimensional melt depth, (u_r, u_θ, u_z), (j_r, j_θ, j_z), F, p are the velocity, electric current density, electric potential function and pressure, respectively. The quantity U_c is the characteristic velocity for the meridional flow driven by the centrifugal acceleration, and this scale is obtained by a balance between the centrifugal acceleration and the electromagnetic body force. B_0 is a characteristic magnetic flux density of the applied

field, and $|B^*| B_0 \geqslant 0.2$ T everywhere, so that the inertialess approximation is valid in all regions of the melt.

The non-dimensional governing equations for steady isothermal melt flows with an applied non-uniform axisymmetric magnetic field and with all inertial terms neglected, except the centrifugal acceleration, are (with the asterisks now dropped)

$$-\frac{u_\theta^2}{r} = -\frac{\partial p}{\partial r} + B_z j_\theta + M^{-2}\left(\nabla^2 u_r - \frac{u_r}{r^2}\right), \tag{10a}$$

$$0 = B_r j_z - B_z j_r + M^{-2}\left(\nabla^2 u_\theta - \frac{u_\theta}{r^2}\right), \quad 0 = -\frac{\partial p}{\partial z} - B_r j_\theta + M^{-2}\nabla^2 u_z; \tag{10b, c}$$

$$j_r = -\frac{\partial F}{\partial r} + B_z u_\theta, \quad j_\theta = B_r u_z - B_z u_r, \quad j_z = -\frac{\partial F}{\partial z} - B_r u_\theta; \tag{11a–c}$$

$$\frac{1}{r}\frac{\partial}{\partial r}(r u_r) + \frac{\partial u_z}{\partial z} = 0; \tag{12}$$

$$\frac{1}{r}\frac{\partial}{\partial r}(r j_r) + \frac{\partial j_z}{\partial z} = 0; \tag{13}$$

where

$$\nabla^2 = \frac{\partial^2}{\partial r^2} + \frac{1}{r}\frac{\partial}{\partial r} + \frac{\partial^2}{\partial z^2} \tag{14}$$

and

$$M = B_0 R_c \left(\frac{\sigma}{\rho_0 \nu}\right)^{\frac{1}{2}} \tag{15}$$

is the Hartmann number. Here, ν is the kinematic viscosity.

For $M \gg 1$ (with $B_0 = 0.2$ T, $M = 718$), the melt can be subdivided into (a) two inviscid core regions, (b) Hartmann layers with $O(M^{-1})$ thickness adjacent to the crystal face, free surface and crucible surfaces, and (c) an interior or free shear layer, which has an $O(M^{-\frac{1}{2}})$ thickness, which lies along the magnetic field line through the point $r = a$ and $z = b$, where the crystal face and the free surface meet, and which separates the inner and the outer inviscid core regions. For a particular magnetic field configuration, these subregions are shown in figure 1(b). Here, a is the non-dimensional crystal radius. For a uniform axial magnetic field, $B_r = 0$ and $B_z = 1$, so that the inner and outer core regions occupy $0 \leqslant r < a$ and $a < r \leqslant 1$ respectively. For an axial field with $B_0 \geqslant 0.2$ T, Langlois, Hjellming & Walker (1987) compared the asymptotic solutions of HWI for large Hartmann number with numerical simulations which incorporated the inertial acceleration terms. It was shown that the principal deviation between the asymptotic solutions and the full numerical solutions is due to the neglect of the second-order perturbation term in the azimuthal velocity solution. Including the inertial terms does not significantly alter the flow pattern for $B_0 \geqslant 0.2$ T. For a shaped field, the minimum field strength is 0.2 T, and use of the large-Hartmann-number and inertialess approximations are justified.

In each core region, for a uniform axial field, (10b) indicates that $j_r = 0$, neglecting the $O(M^{-2})$ viscous terms; (13) indicates that j_z is a function only of r, and (11c) gives F as a linear function of z. Equation (11a) gives the azimuthal velocity as the radial derivative of F and thus u_θ is linear in z. All of the core variables can be expressed in terms of a few integrations of functions of r which are determined by matching with the Hartmann-layer solutions.

For a general non-uniform axisymmetric field, (10b) indicates that $B_r j_z - B_z j_r = 0$, neglecting $O(M^{-2})$ viscous terms, which means that there is no meridional electric

current density in the inviscid core regions perpendicular to magnetic field lines.
Since the meridional electric current density in the core must be along magnetic field
lines, continuity of current (13) requires that the magnitude of the electric current
density along each field line varies inversely as $2\pi r$ times the distance between
magnetic field lines, where the latter is inversely proportional to the local
dimensionless magnetic field strength, $B(r, z) = (B_r^2 + B_z^2)^{\frac{1}{2}}$. If $(11\,a, c)$ are combined to
obtain the meridional components of Ohm's law parallel and perpendicular to a local
magnetic field line, then the parallel component of the electric current density does
not involve u_θ. This can be integrated to obtain the values of F as an integral of the
electric current density parallel to a magnetic field line. The perpendicular component
of Ohm's law then shows that u_θ is the derivative of F in the direction normal to the
field line.

It is this behaviour of the inviscid core variables which we shall exploit in the
analysis of the inviscid core regions for the shaped magnetic field. To do this, a special
orthogonal curvilinear coordinate system is introduced: (Ψ, θ, Φ), where $\Psi(r, z)$ and
$\Phi(r, z)$ are a stream function and potential function for the magnetic field. If
the magnetic field is a uniform axial field, $\Psi = \frac{1}{2}r^2$ and $\Phi = z$, the magnetic
field coordinates coincide with the cylindrical coordinate system. The magnetic
field coordinates will be used for the inviscid core and free shear layer, but
cylindrical coordinates will be used for the Hartmann layers since the normal
boundary coordinate to be stretched is z. Transformations between the two coordinate
systems are needed whenever the core and free shear layer solutions are matched
with the Hartmann-layer solutions.

Orthogonal curvilinear coordinate system based on magnetic field configuration

Using (2) and (3), we define the dimensionless magnetic stream function, $\Psi(r, z)$, and
the dimensionless magnetic potential function $\Phi(r, z)$, where

$$B_r = \frac{\partial \Phi}{\partial r} = -\frac{1}{r}\frac{\partial \Psi}{\partial z}, \tag{16\,a, b}$$

$$B_z = \frac{\partial \Phi}{\partial z} = \frac{1}{r}\frac{\partial \Psi}{\partial r}. \tag{17\,a, b}$$

Since surfaces of constant Ψ and Φ values are mutually orthogonal, we define a right-
handed orthogonal curvilinear coordinate system with (Ψ, θ, Φ). Following Morse &
Feshbach (1953), the metrics for the new coordinate system are

$$h_\Psi = 1/rB, \quad h_\theta = r, \quad h_\Phi = 1/B. \tag{18\,a–c}$$

The unit vectors, perpendicular to constant coordinate surfaces are given by

$$\hat{\boldsymbol{\Psi}} = (B_z/B)\,\hat{\boldsymbol{r}} - (B_r/B)\,\hat{\boldsymbol{z}}, \tag{19}$$

$$\hat{\boldsymbol{\Phi}} = (B_r/B)\,\hat{\boldsymbol{r}} + (B_z/B)\,\hat{\boldsymbol{z}}. \tag{20}$$

The unit vectors for the cylindrical coordinate system are then

$$\hat{\boldsymbol{r}} = (B_z/B)\,\hat{\boldsymbol{\Psi}} + (B_r/B)\,\hat{\boldsymbol{\Phi}}, \tag{21}$$

$$\hat{\boldsymbol{z}} = -(B_r/B)\,\hat{\boldsymbol{\Psi}} + (B_z/B)\,\hat{\boldsymbol{\Phi}}. \tag{22}$$

In the new (Ψ, θ, Φ) coordinate system, $\boldsymbol{B} = B(\Psi, \Phi)\,\hat{\boldsymbol{\Phi}}$. Formally, for any set of
current-carrying solenoids, the functions $B(\Psi, \Phi)$, $B_r(\Psi, \Phi)$, $B_z(\Psi, \Phi)$, $r(\Psi, \Phi)$ and
$z(\Psi, \Phi)$ are known, as are $B(r, z)$, $B_r(r, z)$, $B_z(r, z)$, $\Psi(r, z)$ and $\Phi(r, z)$.

The governing non-dimensional equations in the (Ψ, θ, Φ) coordinate system are

$$-\left(\frac{\partial r}{\partial \Psi}\right)u_\theta^2 = -r\frac{\partial p}{\partial \Psi} + j_\theta + M^{-2}\left\{rB\frac{\partial}{\partial \Psi}\left(B^2\frac{\partial}{\partial \Psi}\left(\frac{r}{B}u_\Psi\right)\right)\right.$$

$$\left. +\frac{B}{r}\frac{\partial}{\partial \Phi}\left(r^2B^2\frac{\partial}{\partial \Phi}\left(\frac{u_\Psi}{rB}\right)\right) - 2rB^2\left(\frac{\partial B}{\partial \Psi}\right)\frac{\partial}{\partial \Phi}\left(\frac{u_\Phi}{B}\right) - 2B^2\frac{\partial}{\partial \Phi}(rB)\frac{\partial}{\partial \Psi}\left(\frac{u_\Phi}{B}\right)\right\}, \quad (23a)$$

$$0 = -j_\Psi + M^{-2}\left\{rB^2\frac{\partial^2}{\partial \Psi^2}(ru_\theta) + rB^2\frac{\partial}{\partial \Phi}\left(\frac{1}{r^2}\frac{\partial}{\partial \Phi}(ru_\theta)\right)\right\}, \quad (23b)$$

$$-\frac{1}{r}\left(\frac{\partial r}{\partial \Phi}\right)u_\theta^2 = -\frac{\partial p}{\partial \Phi} + M^{-2}\left\{B\frac{\partial}{\partial \Psi}\left(r^2B^2\frac{\partial}{\partial \Psi}\left(\frac{u_\Phi}{B}\right)\right)\right.$$

$$\left. +B\frac{\partial}{\partial \Phi}\left(B^2\frac{\partial}{\partial \Phi}\left(\frac{u_\Phi}{B}\right)\right) + B\frac{\partial}{\partial \Psi}\left(2u_\Psi\frac{\partial}{\partial \Phi}(rB)\right) - B\frac{\partial}{\partial \Phi}\left(2ru_\Psi\frac{\partial B}{\partial \Psi}\right)\right\}; \quad (23c)$$

$$\frac{\partial}{\partial \Psi}\left(\frac{r}{B}u_\Psi\right) + \frac{\partial}{\partial \Phi}\left(\frac{u_\Phi}{B}\right) = 0; \quad (24)$$

$$\frac{\partial}{\partial \Psi}\left(\frac{r}{B}j_\Psi\right) + \frac{\partial}{\partial \Phi}\left(\frac{j_\Phi}{B}\right) = 0; \quad (25)$$

$$j_\Psi = -rB\frac{\partial F}{\partial \Psi} + Bu_\theta, \quad j_\theta = -Bu_\Psi, \quad j_\Phi = -B\frac{\partial F}{\partial \Phi}. \quad (26a\text{--}c)$$

The boundary conditions on the velocity $\boldsymbol{u}$, electric density $\boldsymbol{j}$, and electric potential F, of the model CZ system are most easily expressed in terms of cylindrical coordinates. The quartz crucible is an electrical insulator, as is the atmosphere above the free surface, and the boundary conditions at these surfaces are

$$u_r = u_z = j_z = 0, \quad u_\theta = r \quad \text{at} \quad z = 0, \quad 0 \leqslant r \leqslant 1; \quad (27a\text{--}d)$$

$$u_r = u_z = j_r = 0, \quad u_\theta = 1 \quad \text{at} \quad r = 1, \quad 0 \leqslant z \leqslant b + f(1); \quad (28a\text{--}d)$$

$$u_n = j_n = \frac{\partial u_\theta}{\partial n} = \frac{\partial u_t}{\partial n} = 0 \quad \text{at} \quad z = b + f(r), \quad a \leqslant r \leqslant 1, \quad (29a\text{--}d)$$

where $f(r)$ is governed by

$$f - Bn\left\{1 + \left(\frac{\mathrm{d}f}{\mathrm{d}r}\right)^2\right\}^{-\frac{3}{2}}\frac{\mathrm{d}^2f}{\mathrm{d}r^2} = Fr\left\{p - M^{-2}\frac{\partial u_n}{\partial n}\right\}. \quad (29e)$$

Here, n and t denote the coordinates normal and tangential to the free surface in the meridional planes. Two additional non-dimensional parameters are introduced, namely the Bond number, $Bn = \gamma_0/\rho_0 gR_c^2$, and the Froude number, $Fr = \Omega^2 R_c/g$, where γ_0 is the surface tension of the melt. The shear stresses and the pressure variations in the atmosphere above the free surface negligible and for typical speeds of rotation, $Fr \ll 1$. Growth of a constant-diameter crystal is associated with a certain free-surface slope at the crystal edge and $(29e)$ could be solved for the free-surface shape with $\mathrm{d}f/\mathrm{d}r$ given at $r = a$. However, we use the traditional bulk flow approximation which ignores the meniscus near the crystal edge, so that $f = 0$, $n = z$ and $t = r$. In the bulk flow approximation, the crystal–melt interface is assumed flat and coplanar with the flat free surface.

The last boundary which needs to be considered is the crystal face. By taking the

depth as constant, with no melt depletion, the velocity boundary conditions at the crystal face are

$$u_r = u_z = 0, \quad u_\theta = \epsilon r \quad \text{at} \quad z = b, \quad 0 \leqslant r \leqslant a. \tag{30a–c}$$

Here, $\epsilon \Omega$ is the angular velocity of the crystal, with $\epsilon < 0$ indicating rotation of the crystal and crucible in opposite directions.

The electrical conductivity of the crystal, σ_s, near the melting temperature of silicon is on the order of 3% of the electrical conductivity of the melt, with $\delta = \sigma_\mathrm{s}/\sigma = 0.0316$. In most studies on magnetic CZ in an axial field, this small crystal conductivity is neglected and the crystal is treated as an electrical insulator. However, in HWI, it is shown that the resistance of the crystal is comparable to the resistance of the thin Hartmann layer at the crystal face, and the crystal and the Hartmann layer act as resistors in parallel. By including the crystal as part of the entire electric circuit of the system, the melt motion will be strongly dependent on the local ratio of the resistivities of the crystal and Hartmann layer and the ratio of the angular velocities of the crystal and crucible, ϵ. In our asymptotic solution for $M \gg 1$, we assume that δ is comparable to M^{-1}.

In the crystal, the governing dimensional equations for the electric current density, $\boldsymbol{j}_\mathrm{s}$ and electric potential function F_s are

$$\boldsymbol{j}_\mathrm{s} = \delta \sigma \{ -\boldsymbol{\nabla} F_\mathrm{s} + (\epsilon \Omega r \hat{\boldsymbol{\theta}} \times \boldsymbol{B}) \}, \tag{31}$$

$$\boldsymbol{\nabla} \cdot \boldsymbol{j}_\mathrm{s} = 0, \tag{32}$$

where the dimensional azimuthal velocity in the crystal is $\epsilon \Omega r$. Using the same scalings (4)–(9) for the crystal variables as are used for the melt variables, the non-dimensional governing equations are (with asterisks dropped)

$$j_{r\mathrm{s}} = \delta \left(-\frac{\partial F_\mathrm{s}}{\partial r} + B_z \epsilon r \right), \quad j_{\theta\mathrm{s}} = 0, \quad j_{z\mathrm{s}} = \delta \left(-\frac{\partial F_\mathrm{s}}{\partial z} - B_r \epsilon r \right); \tag{33a–c}$$

$$\frac{1}{r} \frac{\partial}{\partial r} (r j_{r\mathrm{s}}) + \frac{\partial j_{z\mathrm{s}}}{\partial z} = 0. \tag{34}$$

Equivalently, we may write the non-dimensional form of (31) and (32) in the (Ψ, θ, Φ) coordinate system as

$$\frac{\partial}{\partial \Psi} \left(\frac{r}{B} j_{\Psi\mathrm{s}} \right) + \frac{\partial}{\partial \Phi} \left(\frac{1}{B} j_{\Phi\mathrm{s}} \right) = 0, \tag{35}$$

$$j_{\Psi\mathrm{s}} = \delta \left(-rB \frac{\partial F_\mathrm{s}}{\partial \Psi} + \epsilon r B \right), \quad j_{\Phi\mathrm{s}} = -\delta B \frac{\partial F_\mathrm{s}}{\partial \Phi}, \quad j_{\theta\mathrm{s}} = 0. \tag{36a–c}$$

With an insulating atmosphere surrounding the crystal, the boundary conditions are

$$j_{r\mathrm{s}} = 0 \quad \text{at} \quad r = a, \quad z \geqslant b, \tag{37a}$$

$$j_{z\mathrm{s}} = j_z, \quad F_\mathrm{s} = F \quad \text{at} \quad z = b, \quad 0 \leqslant r \leqslant a, \tag{37b, c}$$

$$j_\mathrm{s} \to 0 \quad \text{as} \quad z \to \infty, \tag{37d}$$

The conditions (37b, c) prescribe the continuity of the normal current and voltage across the crystal–melt interface, while condition (37a) states that there is no normal current leaving the crystal. Condition (37d) assumes an infinitely long crystal, but most of the electric current is confined to a small portion of the crystal near the crystal–melt interface, and the electric current sees a crystal with an effectively infinite vertical extent, as shown in HWI.

We present solutions for each significant subregion: (i) inner inviscid core, (o) outer inviscid core, (f) free shear layer or interior layer along the magnetic field line $\Psi_{ab} = \Psi(r = a, z = b)$, (t) top Hartmann layer adjacent to the crystal face, (b) bottom Hartmann layer adjacent to the crucible bottom, and (s) crystal. Solutions in adjacent subregions are matched. The solutions for the Hartmann layer at the free surface and the vertical crucible wall are straightforward. The azimuthal problem governing u_θ, j_Ψ, j_Φ and F is decoupled from the meridional problem involving u_Ψ, u_Φ, j_θ and p, with the former providing the driving centrifugal force for meridional melt motion.

3. Azimuthal problem

The variables u_θ, F, and the meridional electric current density (j_r, j_z) or (j_Ψ, j_Φ) are governed by (10b), (11a, c), (13), (23b), (25), (26a, c) and (33)–(36) with boundary conditions (27c, d), (28c, d), (29b, c), (30c) and (37).

We consider first the inviscid core regions where $O(M^{-2})$ terms are neglected. The modified governing equations in (Ψ, θ, Φ) are used. The core variables are written as asymptotic expansions such as $F = F_c + M^{-1}F_c^1 + O(M^{-2})$ where c = i or o to denote inner or outer core, respectively. There are no $O(1)$ meridional electric currents in the core regions, since the meridional electric current must flow along magnetic field lines, and each magnetic field line intersects two Hartmann layers, which can only match an $O(M^{-1})$ normal core current. Each Hartmann layer either satisfies the condition that there is zero normal current at a crucible boundary or at the free surface, or matches the $O(M^{-1})$ normal current in the crystal. The jump in normal current across a Hartmann layer is at most $O(M^{-1})$. Thus the $O(1)$ core solutions are

$$F_c = L_c(\Psi), \quad u_{\theta c} = r \, \mathrm{d}L_c/\mathrm{d}\Psi, \quad j_{\Psi c} = j_{\Phi c} = 0. \tag{38a–d}$$

Here, $r = r(\Psi, \Phi)$. The $O(M^{-1})$ core solutions are

$$F_c^1 = L_c^1(\Psi) - (\Phi - \Phi_0)\, G_c^1(\Psi), \quad u_{\theta c}^1 = r\frac{\mathrm{d}L_c^1}{\mathrm{d}\Psi} - r(\Phi - \Phi_0)\frac{\mathrm{d}G_c^1}{\mathrm{d}\Psi}, \tag{39a, b}$$

$$j_{\Psi c}^1 = 0, \quad \mathrm{j}_{\Phi c}^1 = BG_c^1. \tag{39c, d}$$

The functions L_c^1 and G_c^1 are functions only of Ψ, $\Phi_0 = \Phi(r_0, z_0)$ is some reference value of Φ, and the non-dimensional magnetic field magnitude is $B = B(\Psi, \Phi)$. From (38a, b) we can see that the $O(1)$ angular velocity in the core region is constant along magnetic field lines, where

$$\omega_c(\Psi) = (u_{\theta c}/r) = \mathrm{d}L_c/\mathrm{d}\Psi. \tag{40a}$$

This corresponds to the axial field case where ω_c depends only on the radial coordinate. The solutions (39a, b) indicate that the $O(M^{-1})$ angular velocity varies linearly with Φ along each magnetic field line, such that

$$\omega_c^1(\Psi, \Phi) = \mathrm{d}L_c^1/\mathrm{d}\Psi - (\Phi - \Phi_0)\,\mathrm{d}G_c^1/\mathrm{d}\Psi. \tag{40b}$$

From (10b) and (13), which determine the $O(M^{-1})$ meridional current density, an electric current stream function in the core may be defined such that

$$j_{rc}^1 = -\frac{1}{r}\frac{\partial h_c^1}{\partial z}, \quad j_{zc}^1 = \frac{1}{r}\frac{\partial h_c^1}{\partial r}, \tag{41a, b}$$

where
$$h_c^1(r, z) = H_c^1(\Psi) \quad \text{with} \quad G_c^1 = \mathrm{d}H_c^1/\mathrm{d}\Psi. \tag{42}$$
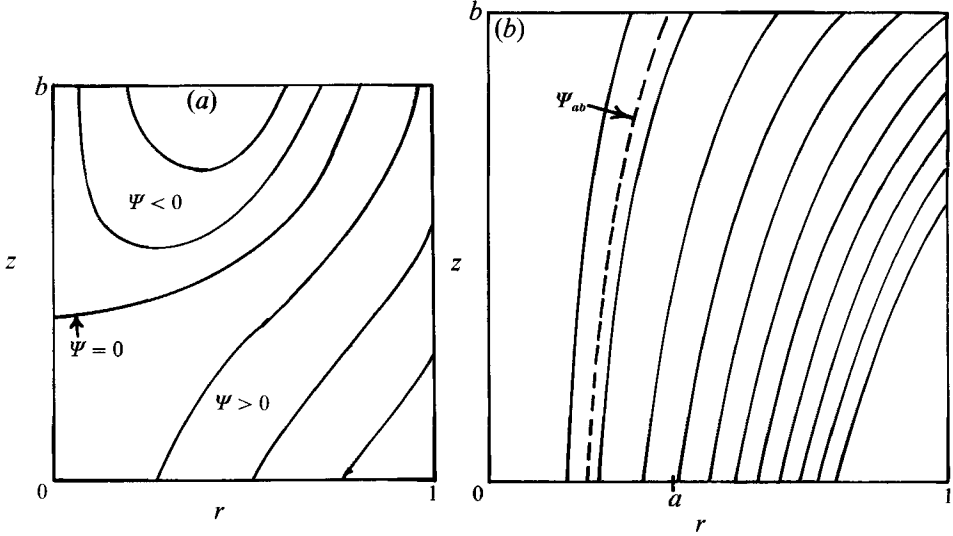
FIGURE 2. (a) Sketch of field case I, for which no magnetic field lines contact both the crystal and crucible. (b) Sketch of field case II, for which there are magnetic field lines which contact both the crystal and crucible.

The jump in azimuthal velocity across each Hartmann layer determines the meridional electric current density in the layer and the adjacent core region. If there is an axial variation of u_θ across the boundary layer on the crystal face, crucible bottom or free surface, a component of the electromagnetic body force is required to balance the viscous shearing in that boundary layer. In the axial field case, the only jumps in u_θ occur across the top and bottom Hartmann layers adjacent to the inner core and the free shear layer separating the two core regions, with the entire outer region rotating as a rigid body with the crucible. For the shaped field, the field configuration determines the regions of rigid-body rotation, and the Hartmann layers and free shear layer where the jumps in u_θ occur. We shall consider several possible model field configurations which limit the types of configurations that need to be evaluated. These cases are illustrated in figure 2.

3.1. *Field case I*

For the 'cusp' field configuration, shown in figure 2(a), there are no magnetic field lines which are in contact with both the crystal and the crucible. We consider first the region bounded by magnetic field lines which contact the free surface and crystal. At the free surface there can be no jump in u_θ, and so there is no electric current generated. Thus, there will be no $O(M^{-1})$ electric current density along these field lines. Since these field lines also contact the crystal, there may be no jump in u_θ between the core region and crystal face, since any current generated has no means to complete the circuit path. Therefore, the region bounded by the field lines which contact only the crystal and free surface must rotate as a rigid body with the crystal. The solutions in this entire region to $O(M^{-2})$ are

$$F_{\mathrm{i}} = \epsilon \Psi, \quad u_{\theta \mathrm{i}} = \epsilon r, \quad j_{\Psi \mathrm{i}} = j_{\Phi \mathrm{i}} = 0. \qquad (43a\text{–}d)$$

The solutions (43) are also the solutions in the crystal. A similar analysis can be made for the region bounded by the field lines which have only crucible–crucible or

crucible–free surface contact. This region rotates as a rigid body with the crucible, and the solutions to $O(M^{-2})$ are

$$F_0 = \Psi, \quad u_{\theta 0} = r, \quad j_{\Psi 0} = j_{\Phi 0} = 0. \tag{44a–d}$$

These two regions of different rigid-body rotation are separated by a free shear layer lying along a magnetic streamline which extends from a point at $r = 0$ where $\boldsymbol{B} = 0$ to the free surface. Then $\Psi = 0$ on this separation field line, the electric potential F is continuous here, and Ψ has opposite signs in the two regions. This free shear layer is similar to that to be discussed for field case II.

3.2. *Field case II*

For this field configuration sketched in figure 2 (*b*), there are two separate regions: (i) a region with field lines which contact both the crystal and crucible, and (ii) a region where the field lines have crucible–crucible or free surface–crucible contacts. For the latter region, the solutions are given by the rigid-body rotation solutions (44).

The region of interest is that defined by the magnetic field lines which contact both the crystal and crucible. The crucible rotates with a normalized angular velocity of one and the crystal rotates with a normalized angular velocity of ϵ. Since the $O(1)$ angular velocity in the inner core, ω_i, is constant along magnetic field lines, there must be an $O(1)$ variation of u_θ through the Hartmann layers between the inviscid core and the bounding surfaces. We define the inner core region to be the region bounded by the centreline, crystal face, crucible bottom and $\Psi_{ab} = \Psi(r = a, z = b)$, where Ψ_{ab} is the dividing magnetic streamline. If B is decreasing or increasing as z increases, the magnetic field line Ψ_{ab} will intersect the crucible bottom at $r < a$ or $r > a$, respectively. The inner core solutions are those given in (38) and (39).

As a preliminary step in the analysis of this region, it is useful to define several functions which relate the variable dependence on (Ψ, Φ) to the variable dependence on (r, z). For the magnetic streamlines $0 \leqslant \Psi \leqslant \Psi_{ab}$, we identify these by their radial coordinate r at $z = b$. Then the interval $0 \leqslant \Psi(r, b) \leqslant \Psi_{ab}$ corresponds to the interval $0 \leqslant r \leqslant a$ at $z = b$. Next, we define $R(r)$ as the radial coordinate at $z = 0$ of the magnetic streamline whose radial coordinate is r at $z = b$, where

$$\Psi(R(r), 0) = \Psi(r, b) \quad \text{for} \quad 0 \leqslant r \leqslant a, \tag{45a}$$

$$\frac{R}{r}\frac{\mathrm{d}R}{\mathrm{d}r} = \frac{B_z(r, b)}{B_z(R, 0)}. \tag{45b}$$

Throughout the analysis we will use R to denote the radial coordinate at $z = 0$ which corresponds to r at $z = b$, where 'corresponds' means along the same magnetic streamline.

The last quantity is $\rho(r, z)$ which is the radial coordinate for $0 \leqslant z \leqslant b$ of the magnetic streamline whose radial coordinate is r at $z = b$. Thus,

$$\Psi(\rho, z) = \Psi(r, b) \quad \text{for} \quad 0 \leqslant r \leqslant a \quad \text{and} \quad 0 \leqslant z \leqslant b; \tag{46a}$$

$$\rho(r, b) = r, \quad \rho(r, 0) = R, \tag{46b, c}$$

$$\frac{\rho}{r}\frac{\partial \rho}{\partial r} = \frac{B_z(r, b)}{B_z(\rho, z)}, \quad \frac{\partial \rho}{\partial z} = \frac{B_r(\rho, z)}{B_z(\rho, z)}. \tag{46d, e}$$

For the analysis of the Hartmann layers, we shall assume that all magnetic streamlines intersecting the crystal face also intersect the crucible bottom, but the analysis can be generalized to the case where some of these magnetic streamlines intersect the vertical crucible wall. If there is a region in which the magnetic

streamlines $\Psi_{10} \leqslant \Psi \leqslant \Psi_{ab}$ intersect the vertical wall, where $\Psi_{10} = \Psi(r = 1, z = 0)$, a stretching of the radial coordinate and solving for the boundary layer variables is accomplished in a similar manner to that described below. Matching of the two $O(M^{-1})$ boundary layers is done by looking at the intersection region at $r = 1, z = 0$, which is an $O(M^{-1}) \times O(M^{-1})$ region.

For the Hartmann layer on the crucible bottom, $0 \leqslant r \leqslant R(a)$, the axial coordinate is stretched by substituting $Z = Mz$. We stretch (10b), (11a, c) and (13). In the bottom Hartmann layer (denoted by the subscript b), j_{rb}, $u_{\theta b}$ and F_b are $O(1)$, while the leading-order axial current is the $O(M^{-1})j_{zb}^1$. The magnetic field must also be expanded in an asymptotic series, where

$$B_{rb}(r, Z) = B_r(r, 0) + \frac{Z}{M}\frac{\partial B_r}{\partial z}\bigg|_{(r, 0)} + O(M^{-2}), \qquad (47a)$$

$$B_{zb}(r, Z) = B_z(r, 0) + \frac{Z}{M}\frac{\partial B_z}{\partial z}\bigg|_{(r, 0)} + O(M^{-2}). \qquad (47b)$$

There are no perturbations to the applied magnetic field.

After coordinate stretching, (11c) gives

$$F_b(r, Z) = L_i(r, 0) = L_i(\Psi(r, 0)). \qquad (48)$$

The stretched equations (10b) and (11a) govern j_{rb} and $u_{\theta b}$. The solutions which satisfy the boundary condition (27d) and which match the solutions (38) are

$$u_{\theta b}(r, Z) = \{r - u_{\theta i}(r, 0)\}\exp\left(-ZB_z(r, 0)\right) + u_{\theta i}(r, 0), \qquad (49a)$$

$$j_{rb}(r, Z) = B_z(r, 0)\{r - u_{\theta i}(r, 0)\}\exp\left(-ZB_z(r, 0)\right). \qquad (49b)$$

The stretched equation (13) with (41b), (42) and (49b) yields j_{zb}^1 and the $O(M^{-1})$ current stream function, h_i^1 in the core at $z = 0$, where

$$j_{zb}^1(r, Z) = \frac{1}{r}\frac{\partial}{\partial r}(r^2 - ru_{\theta i}(r, 0))\left(\exp\left(-ZB_z(r, 0)\right) - 1\right)$$

$$\qquad - \frac{Z}{r}(r^2 - ru_{\theta i}(r, 0))\frac{dB_z(r, 0)}{dr}\exp\left(-ZB_z(r, 0)\right), \quad (49c)$$

$$h_i^1(R, 0) = h_i^1(r, b) = H_i^1(\Psi) = R^2(\omega_i(\Psi) - 1). \qquad (50)$$

The axial current in the bottom Hartmann layer has an additional term that is not present in the uniform axial field case, which is linear in Z and proportional to the variation in the axial magnetic field in the radial direction. This term represents an internal, vertical redistribution of the radial current as the local boundary thickness changes inversely with $B_z(r, 0)$.

In the inner core, the values of the $O(M^{-1})$ electric current streamfunction H_i^1 and the $O(1)$ angular velocity $\omega_i = u_{\theta i}/r$ are constant along each magnetic field line, $\Psi = $ constant. The magnetic field line Ψ through the point (r, b) intersects the bottom at $(R, 0)$ where the jump in azimuthal velocity across the bottom Hartmann layer is $R(\omega_i(\Psi) - 1)$. A radial current is required to produce the azimuthal component of the electromagnetic body force to balance the shear stresses in this jump. This radial current must enter the bottom Hartmann layer from the core between $r = 0$ and $r = R$. It is this balance which leads to the condition (50) relating the current stream function H_i^1 and $\omega_i(\Psi)$.

For the Hartmann layer on the crystal face, the axial coordinate is stretched by substituting $Z' = M(z - b)$. The magnetic field is expanded in a manner similar to that

in (47). The solutions in the top Hartmann layer (denoted by subscript t), which satisfy the stretched versions of (10b), (11a, b) and (13), satisfy boundary conditions (30c) and (37b, c), and match the inner core solution (38) are

$$F_t(r, Z') = L_i(r, b) = L_i(\Psi) = F_s(r, b), \tag{51}$$

$$u_{\theta t}(r, Z') = u_{\theta i}(r, b) + (\epsilon r - u_{\theta i}(r, b)) \exp(Z'B_z(r, b)), \tag{52a}$$

$$j_{rt}(r, Z') = B_z(r, b)(\epsilon r - u_{\theta i}(r, b)) \exp(Z'B_z(r, b)), \tag{52b}$$

$$j_{zt}^1(r, Z') = j_{zs}^1(r, b) + \frac{1}{r}\frac{\partial}{\partial r}(\epsilon r^2 - r u_{\theta i}(r, b))(1 - \exp(Z'B_z(r, b)))$$

$$-\frac{Z'}{r}\frac{dB_z(r, b)}{dr}(\epsilon r^2 - r u_{\theta i}(r, b)) \exp(Z'B_z(r, b)). \tag{52c}$$

Matching the $O(M^{-1})$ axial current and the current stream function h_i^1 yields

$$h_s^1(r, b) = h_i^1(r, b) + r u_{\theta i}(r, b) - \epsilon r^2$$
$$= H_i^1(\Psi) + r^2(\omega_i(\Psi) - \epsilon), \tag{53}$$

where $h_s^1(r, b)$ is the current stream function in the crystal evaluated at the melt–solid interface.

The current stream function in the crystal is determined by solving $\nabla \times j_s = 0$, using the definitions (41) with the subscript c replaced by a subscript s to denote the crystal variable, and with the boundary conditions on h_s^1 derived from conditions (37a), (37d). The boundary value problem for the current stream function in the crystal is

$$r\frac{\partial}{\partial r}\left(\frac{1}{r}\frac{\partial h_s^1}{\partial r}\right) + \frac{\partial^2 h_s^1}{\partial z^2} = 0, \tag{54}$$

$$h_s^1(a, z) = 0, \tag{55a}$$

$$h_s^1(r, z) \to 0 \quad \text{as} \quad z \to \infty, \tag{55b}$$

$$h_s^1(r, b) - \frac{(R^2 + r^2)}{\delta M r^2 B_z(r, b)}\left(\frac{\partial h_s^1(r, b)}{\partial z}\right) = -R^2(1 - \epsilon), \quad 0 \leqslant r \leqslant a. \tag{55c}$$

The condition (55c) is derived using (14), (33a), (38b), (40a), (50) and (53). At each point on the crystal face, the quantity $\gamma(r) = \delta Ma B_z(r, b)$ is the local ratio of the electrical resistances of the crystal and of the top Hartmann layer. The dimensionless crystal resistance is δa, and the local resistance of the Hartmann layer is the product of a dimensionless resistivity of one and the local boundary layer thickness $(MB_z(r, b))^{-1}$. This ratio is taken to be $O(1)$ for all r. The separation of variables solution for (54), (55) is

$$h_s^1(r, z) = r\sum_{n=1}^{\infty} A_n J_1\left(\frac{X_n r}{a}\right) \exp\left(-\frac{X_n(z - b)}{a}\right), \tag{56}$$

where X_n are the zeros of J_1, J_1 being the first-order Bessel function of the first kind. The coefficients A_n are found by satisfying the boundary condition (55c), for a given magnetic field configuration.

In order to determine the $O(1)$ electric potential in the crystal, (33a, c) are rewritten as

$$\frac{\partial F_s}{\partial r} = \epsilon r B_z + \frac{1}{\delta M r}\left(\frac{\partial h_s^1}{\partial z}\right), \quad \frac{\partial F_s}{\partial z} = -\epsilon r B_r - \frac{1}{\delta M r}\left(\frac{\partial h_s^1}{\partial r}\right). \tag{57, 58}$$

Using (56) and (14), the $O(1)$ electric potential in the crystal is

$$F_s(r, z) = \epsilon \Psi + \frac{1}{\delta M} \sum_{n=1}^{\infty} A_n J_0\left(\frac{X_n r}{a}\right) \exp\left(-\frac{X_n(z-b)}{a}\right). \tag{59}$$

Within the crystal, the imbalance between the $O(1)$ electric potential and the induced potential due to the interaction of the rotating crystal and the magnetic field, drives an $O(\delta)$ electric current which is small.

If the crystal is treated as an electrical insulator, with a parametric limit of $\gamma = \delta M a B_z(r, b) \ll 1$, then all of the electric current flows through the top Hartmann layer, and the net radial currents inside the top Hartmann layer at r and inside the bottom Hartmann layer at $R(r)$ must be equal and opposite. The inner core angular velocity for the limit $\gamma \ll 1$ is obtained by combining (50), (53) with $h_s^1(r, b) = 0$, such that

$$\omega_i(\Psi) = \frac{R^2 + \epsilon r^2}{R^2 + r^2}.$$

For a uniform axial magnetic field with $\gamma \ll 1$, then $R = r$, $\omega_i = \frac{1}{2}(1 + \epsilon)$ and the inner core rotates as a rigid body with the average angular velocity of the crystal and crucible. In the shaped field case, if the magnetic field lines are spreading radially as z increases from 0 to b, then $R < r$ and $\omega_i(\Psi)$ will be closer to ϵ, the angular velocity of the crystal. If the magnetic field lines converge radially as z increases from 0 to b, then $\omega_i(\Psi)$ will be closer to 1, the angular velocity of the crucible. The angular velocity on each magnetic field lines is an area-weighted average of the crucible and crystal rotation rates, where the areas are those inside the field line at $z = 0$ and $z = b$, respectively. In general, the ratio $R(r)/r$ varies with r for $0 \leqslant r \leqslant a$, so that the inner core azimuthal motion involves shearing between magnetic field lines with different angular velocities $\omega_i(\Psi)$.

If the crystal presents the lower resistance path with the parametric limit $\gamma \gg 1$, then all of the current will enter the crystal, with no radial current in the top Hartmann layer. Because the radial current flux through the Hartmann layer is related to the jump in the azimuthal velocity, there can be no jump in u_θ from the inner core to the crystal, and the inner core will then rotate as a rigid body with the crystal, $u_{\theta i} = \epsilon r$, and $\omega_i(\Psi) = \epsilon$.

When the magnetic field is a uniform axial field, the value of γ is constant across the crystal face for a given magnetic field strength. For the shaped field case II, γ may be a function of r, as the ratio of the local resistances of the top Hartmann layer and crystal depends on the local value of the axial field strength. For finite non-zero values of γ, the angular velocity along each magnetic field line lies between the two values corresponding to the parametric limits $\gamma \gg 1$, where $\omega_i(\Psi) = \epsilon$, and $\gamma \ll 1$, where $\omega_i(\Psi) = (R^2 + \epsilon r^2)/(R^2 + r^2)$, and no $O(1)$ rigid-body motion is possible in the inner core region. By treating the crystal as a slight electrical conductor, with a resistance comparable to the top Hartmann layer, the amount of electric current entering the crystal varies between 0 (crystal is an electrical insulator) and $(1 - \epsilon)R^2$ (crystal is the lower-resistance path). Since the inner core azimuthal velocity is determined by the jump in electric current across the top Hartmann layer, the flow behaviour is highly dependent on the electric circuit model of the crystal and top Hartmann layer. It is this property which may allow for tailored centrifugal pumping flows along the crystal face, flows which are considered in the next section.

The inner core azimuthal velocity for finite non-zero values of γ may be

determined using (50) and (53) or, equivalently, the angular velocity $\omega_i(\Psi)$ can be found, where

$$\omega_i(\Psi) = \left(\frac{u_{\theta i}}{r}\right)_{\Psi=\text{constant}} = \frac{h_s^1(r,b) + \epsilon r^2 + R^2}{R^2 + r^2}. \tag{60}$$

The value of $\omega_i(\Psi)$ on a magnetic streamline $\Psi(r,b)$ for $0 \leqslant r \leqslant a$ fixes the value of ω_i in the inner core at all points along that magnetic streamline $\Psi(\rho,z)$. Some results are presented in §5 for two specific magnetic field configurations.

The free shear layer separates the inner and the outer inviscid cores, and accommodates the jump in the azimuthal velocity across the layer. It is through this layer that the $O(M^{-1})$ electric current density completes its circuit. This current travels down through the inviscid core along magnetic field lines, outward through the bottom Hartmann layer to $R(a)$, up through the free shear layer, and inward from $r = a$ through the crystal and top Hartmann layer as parallel paths back into the core at $z = b$. The current will circulate in the opposite direction for certain values of ϵ. To $O(M^{-2})$, there is no current circulation in the outer region where the magnetic field lines have only crucible–free surface and crucible–crucible contacts.

For the axial field case, the free shear layer is located at $r = a$, and the radial coordinate is stretched. For the shaped field, the free shear layer exists along the separating magnetic streamline $\Psi = \Psi(r = a, z = b) = \Psi_{ab}$. If the solutions for the free shear layer are sought using cylindrical coordinates, both the axial and the radial coordinates must be stretched. As this is a cumbersome task, the governing equations (23b), (25) and (26) in the (Ψ, θ, Φ) coordinate system are used, with the coordinate stretching $\xi = M^{\frac{1}{2}}(\Psi - \Psi_{ab})$. The free shear layer variables (denoted by subscript f) are

$$j_{\Psi f} = M^{-1}j_{\Psi f}^1 + O(M^{-\frac{3}{2}}), \quad j_{\Phi f} = M^{-\frac{1}{2}}j_{\Phi f}^0 + O(M^{-1}), \tag{61a,b}$$

$$u_{\theta f} = U_{\theta f} + O(M^{-\frac{1}{2}}), \tag{61c}$$

$$F_f = F_i(\Psi_{ab}) + M^{-\frac{1}{2}}F_f^0 + O(M^{-1}). \tag{61d}$$

In addition to the asymptotic expansions for the flow variables, the radius and magnetic field need to be expressed in the free layer region. Here,

$$r(\xi, \Phi) = r(\Psi_{ab}, \Phi) + M^{-\frac{1}{2}}\xi\left(\frac{\partial r}{\partial \Psi}\right)_{\Psi_{ab}, \Phi} = \tilde{r} + M^{-\frac{1}{2}}\xi\chi, \tag{62a}$$

$$B(\xi, \Phi) = B(\Psi_{ab}, \Phi) + M^{-\frac{1}{2}}\xi\left(\frac{\partial B}{\partial \Psi}\right)_{\Psi_{ab}, \Phi} = \tilde{B} + M^{-\frac{1}{2}}\xi\beta, \tag{62b}$$

where $\tilde{r}(\Phi)$ and $\tilde{B}(\Phi)$ are the radial coordinate and magnetic field strength at each point Φ along the magnetic field line Ψ_{ab}.

The leading-order stretched equations (23b), (25), (26a,c) are

$$\frac{\tilde{r}}{\tilde{B}}\frac{\partial j_{\Psi f}^1}{\partial \xi} + \frac{\partial}{\partial \Phi}\left(\frac{1}{\tilde{B}}j_{\Phi f}^0\right) = 0, \tag{63a}$$

$$-\frac{1}{\tilde{B}}\frac{\partial j_{\Phi f}^0}{\partial \xi} = \frac{\partial}{\partial \Phi}\left(\frac{U_{\theta f}}{\tilde{r}}\right), \tag{63b}$$

$$j_{\Psi f}^1 = (\tilde{B}\tilde{r})^2\frac{\partial^2 U_{\theta f}}{\partial \xi^2}. \tag{63c}$$

Combining (63) with the matching conditions for the inner and outer core gives

$$\tilde{B}\tilde{r}^4 \frac{\partial^4}{\partial \xi^4}\left(\frac{U_{\theta \mathrm{f}}}{\tilde{r}}\right) - \frac{\partial^2}{\partial \Phi^2}\left(\frac{U_{\theta \mathrm{f}}}{\tilde{r}}\right) = 0, \tag{64a}$$

$$U_{\theta \mathrm{f}}/\tilde{r} \rightarrow \omega_\mathrm{i}(\Psi_{ab}), \quad j^0_{\Phi \mathrm{f}} \rightarrow 0, \quad j^1_{\Psi \mathrm{I}} \rightarrow 0 \quad \text{as} \quad \xi \rightarrow -\infty, \tag{64b-d}$$

$$U_{\theta \mathrm{f}}/\tilde{r} \rightarrow 1, \quad j^0_{\Phi \mathrm{f}} \rightarrow 0, \quad j^1_{\Psi \mathrm{I}} \rightarrow 0 \quad \text{as} \quad \xi \rightarrow +\infty. \tag{64e-g}$$

There are three additional conditions which need to be specified in the boundary value problem for $U_{\theta \mathrm{f}}(\xi, \Phi)$. These are the matching conditions with the intersection regions on the bottom ($z = 0$, for all ξ), on the crystal face ($z = b$, $\xi < 0$) and with the free surface ($z = b$, $\xi > 0$). From HWI, the condition on the free surface, for a Froude number which is at most $O(M^{-\frac{1}{2}})$, requires that there is no normal current at the free surface to $O(M^{-\frac{3}{2}})$. Therefore, the boundary condition on the current is

$$j^0_{\Phi \mathrm{f}} = 0 \quad \text{at} \quad z = b \quad \text{for} \quad \xi > 0. \tag{65a}$$

By using the coordinate stretchings $\zeta = M(\Phi - \Phi_\mathrm{b})$, $\zeta' = M(\Phi - \Phi_\mathrm{t})$, where $\Phi_\mathrm{b} = \Phi(r = R(a), z = 0)$ and $\Phi_\mathrm{t} = \Phi(r = a, z = b)$, in addition to the coordinate stretching in Ψ along the Ψ_{ab} line, the equations (23b), (25) and (26a, c) can be solved in the top and bottom intersection regions. The $O(1)$ azimuthal velocity and the $O(1)$ electric current component in the intersection regions, $j_{\Psi \mathrm{I}}$, have the normal exponential structure. Introducing $j_{\Psi \mathrm{I}}$ into the stretched equation (25) gives an equation for the $O(M^{-\frac{1}{2}})$ $j^0_{\Phi \mathrm{I}}$. The matching conditions on $j^0_{\Phi \mathrm{f}}$ at the top and bottom are

$$j^0_{\Phi \mathrm{f}} = R(a)B^{\frac{3}{2}}(\Psi_{ab}, \Phi_\mathrm{b})\frac{\partial U_{\theta \mathrm{f}}}{\partial \xi} \quad \text{at} \quad \Phi_\mathrm{b} \quad \text{for all} \quad \xi, \tag{65b}$$

$$j^0_{\Phi \mathrm{f}} = -aB^{\frac{3}{2}}(\Psi_{ab}, \Phi_\mathrm{t})\frac{\partial U_{\theta \mathrm{f}}}{\partial \xi} \quad \text{at} \quad \Phi_\mathrm{t} \quad \text{for} \quad \xi < 0. \tag{65c}$$

The governing equation and boundary conditions (64), (65) constitute a well-posed boundary value problem for $U_{\theta \mathrm{f}}(\xi, \Phi)$. Since the variable coefficients $\tilde{r}(\Phi)$ and $\tilde{B}(\Phi)$ depend only on Φ, a Fourier transform with respect to ξ reduces the problem to a linear differential equation with variable coefficients. However, this approach leads to an integral equation because of the discontinuity in the boundary condition at Φ_t. Therefore, a purely numerical solution, with special attention to the singularity at $\xi = 0$, $\Phi = \Phi_\mathrm{t}$ may be more efficient. For the discussion in the next section, the important fact is that the free shear layer solution exists in which $U_{\theta \mathrm{f}}$ varies from $\tilde{r}\omega_\mathrm{i}(\Psi_{ab})$ in the inner core to $\tilde{r}$ in the outer core. For the uniform axial magnetic field, $\tilde{r} = a$, $\tilde{B} = 1$ and the solution for the free shear layer problem (64), (65) is a simple error function of $\xi(\Phi_\mathrm{t} - \Phi)^{-\frac{1}{2}} = \xi(b - z)^{-\frac{1}{2}}$. Thus, the transition between the core angular velocities is very abrupt near $z = b$ and gradual near $z = 0$.

4. Meridional motion

The variables (u_r, u_z) or (u_Ψ, u_Φ), j_θ, and p are governed by equations $(10a, c)$, $(11b)$, (12), $(23a, c)$, (24) and $(26c)$, and by the boundary conditions $(27a, b)$, $(28a, b)$, $(29a, d, e)$ and $(30a, b)$. Since the azimuthal velocity has been determined in §3, the centrifugal acceleration term is a known forcing function in the meridional momentum transport equations. There are two cases which need to be considered for the meridional flow solutions corresponding to the two field configurations which yield rigid-body or non-rigid-body azimuthal motion.

4.1. *Field case I*

The magnetic field configuration for this case has two distinct regions of rigid-body motion separated by a free shear layer, with the azimuthal velocity, meridional electric current density and electric potential function given by (43), (44). For the rigid-body motion, the electric potential depends linearly on Ψ, and the angular velocity ω is a constant, either ϵ or 1. For a rigid-body motion, both the azimuthal velocity and the centrifugal acceleration are independent of the magnetic field configuration at any radial position in the melt. This means that a purely radial pressure gradient can exactly balance the centrifugal acceleration, and no component of the Lorentz force is required to balance the centrifugal acceleration. The solutions for the meridional motion in the core regions are

$$u_r = u_z = u_\Psi = u_\Phi = j_\theta = 0, \tag{66a–e}$$

$$p_i = p_s + \tfrac{1}{2}\epsilon r^2 \quad \text{or} \quad p_o = p_c + \tfrac{1}{2}r^2, \tag{66f, g}$$

where p_s and p_c are two different constants. There is discontinuity in pressure across the free shear layer lying along the branch of the $\Psi = 0$ magnetic field line which separates the two core regions. This pressure discontinuity is associated with a strong meridional motion inside the free shear layer with a structure similar to that which is to be discussed for field case II.

4.2 *Field case II*

The outer core region rotates as a rigid body and the solutions (66a–e) apply here. The $O(1)$ inner core solutions are found using the governing equations in (Ψ, θ, Φ), with the $O(M^{-2})$ viscous terms neglected. Here

$$p_i(\Psi, \Phi) = \tfrac{1}{2}(r\omega_i(\Psi))^2 + P_i(\Psi), \tag{67}$$

$$u_{\Psi i} = -\frac{r^3}{2B}\frac{\mathrm{d}}{\mathrm{d}\Psi}(\omega_i^2) - \frac{r}{B}\frac{\mathrm{d}P_i}{\mathrm{d}\Psi}, \tag{68}$$

$$u_{\Phi i} = B\frac{\partial}{\partial\Psi}\left\{\frac{\mathrm{d}}{\mathrm{d}\Psi}(\omega_i^2)\int_{\Phi_0}^{\Phi}\frac{r^4}{2B^2}\mathrm{d}\Phi* + \frac{\mathrm{d}P_i}{\mathrm{d}\Psi}\int_{\Phi_0}^{\Phi}\frac{r^2}{B^2}\mathrm{d}\Phi*\right\} + B\frac{\mathrm{d}A(\Psi)}{\mathrm{d}\Psi}, \tag{69}$$

where $\Phi_0 = \Phi(r_0, z_0)$ is some reference value of Φ, and the angular velocity is given by (60). There are two integration functions, $P_i(\Psi)$ and $A(\Psi)$, which are determined by matching the Hartmann layer solutions. A stream function, G, for the meridional velocity is defined using the continuity equations (12), (24), where

$$u_{\Psi i} = \frac{B}{r}\frac{\partial G}{\partial\Phi}, \quad u_{\Phi i} = -B\frac{\partial G}{\partial\Psi}, \tag{70a, b}$$

$$u_{ri} = \frac{1}{r}\frac{\partial G}{\partial z}, \quad u_{zi} = -\frac{1}{r}\frac{\partial G}{\partial r}, \tag{71a, b}$$

and

$$G(\Psi, \Phi) = G(r, z) = -\frac{\mathrm{d}}{\mathrm{d}\Psi}(\omega_i^2)\int_{\Phi_0}^{\Phi}\frac{r^4}{2B^2}\mathrm{d}\Phi* - \frac{\mathrm{d}P_i}{\mathrm{d}\Psi}\int_{\Phi_0}^{\Phi}\frac{r^2}{B^2}\mathrm{d}\Phi* + A(\Psi). \tag{72}$$

The Hartmann layers match any value of u_{ri} at $z = 0$ and $z = b$ as long as the $O(1)$ inner core solutions satisfies the conditions

$$G(r, 0) = G(\Psi(r, 0), \Phi(r, 0)) = 0 \quad \text{for} \quad 0 \leqslant r \leqslant R(a), \tag{73}$$

$$G(r, b) = G(\Psi(r, b), \Phi(r, b)) = 0 \quad \text{for} \quad 0 \leqslant r \leqslant a. \tag{74}$$

In order to apply the boundary conditions (73), (74) at $z = 0$ and $z = b$ to the velocity stream function G, we introduce

$$G(\Psi, \Phi) = C(\Psi)f_1(\Psi, \Phi) + D(\Psi)f_2(\Psi, \Phi) + A(\Psi), \qquad (75a)$$

where

$$C(\Psi) = -\frac{\mathrm{d}}{\mathrm{d}\Psi}(\omega_1^2(\Psi)), \quad D(\Psi) = -\frac{\mathrm{d}P_1(\Psi)}{\mathrm{d}\Psi}, \qquad (75b, c)$$

$$f_1(\Psi, \Phi) = \int_{\Phi_0}^{\Phi} \frac{\rho^4}{2B^2}\,\mathrm{d}\Phi*, \quad f_2(\Psi, \Phi) = \int_{\Phi_0}^{\Phi} \frac{\rho^2}{B^2}\,\mathrm{d}\Phi*. \qquad (75d, e)$$

Along a given magnetic streamline Ψ, the functions $C(\Psi)$, $D(\Psi)$ and $A(\Psi)$ are constant, and the integrals f_1 and f_2 vary only with Φ. On each magnetic streamline, Φ has particular values at $z = 0$ and $z = b$, denoted by Φ_b and Φ_t, respectively, so that

$$\Phi_b(\Psi) = \Phi(R(r), 0), \quad \Phi_t(\Psi) = \Phi(r, b). \qquad (76)$$

The boundary conditions (73), (74) are then applied along a particular magnetic streamline to the velocity stream function (75a). The solutions for the unknown functions $D(\Psi)$ and $A(\Psi)$ are

$$D(\Psi) = -\frac{C(\Psi)(f_1(\Psi, \Phi_t) - f_1(\Psi, \Phi_b))}{f_2(\Psi, \Phi_t) - f_2(\Psi, \Phi_b)}, \qquad (77a)$$

$$A(\Psi) = -C(\Psi)f_1(\Psi, \Phi_b) - D(\Psi)f_2(\Psi, \Phi_b). \qquad (77b)$$

Using (75), (77), the $O(1)$ velocity stream function (70) may be written

$$G(\Psi, \Phi) = -\frac{\mathrm{d}}{\mathrm{d}\Psi}(\omega_1^2)\left\{ \int_{\Phi_b}^{\Phi} \frac{\rho^4}{2B^2}\,\mathrm{d}\Phi* - \left(\int_{\Phi_b}^{\Phi} \frac{\rho^2}{B^2}\,\mathrm{d}\Phi*\right)\left[\int_{\Phi_b}^{\Phi_t} \frac{\rho^4}{2B^2}\,\mathrm{d}\Phi*\right]\left[\int_{\Phi_b}^{\Phi_t} \frac{\rho^2}{B^2}\,\mathrm{d}\Phi*\right]^{-1}\right\}. \qquad (78a)$$

Using (77a), the pressure, $P_1(\Psi)$, is given by

$$P_1(\Psi) = \int_{\Psi}^{\Psi_{ab}} -\frac{\mathrm{d}}{\mathrm{d}\Psi*}(\omega_1^2)\left[\frac{f_1(\Psi*, \Phi_t) - f_1(\Psi*, \Phi_b)}{f_2(\Psi*, \Phi_t) - f_2(\Psi*, \Phi_b)}\right]\mathrm{d}\Psi* + P_s, \qquad (78b)$$

where P_s is a constant.

For a given non-uniform axisymmetric magnetic field, the $O(1)$ inner core meridional velocities, u_{ri} and u_{zi}, are now completely determined. For a uniform axial magnetic field, $B = 1$, $\rho = r$ and $G = 0$. This axial field case represents a singular limit of a non-uniform field for which the centrifugal acceleration is exactly perpendicular to the magnetic field, the centrifugal acceleration is balanced by a radial pressure gradient, and there is no $O(1)$ meridional circulation. For any magnetic field with a significant radial component, there is a component of the centrifugal acceleration along each magnetic field line, the pressure gradient cannot balance the centrifugal acceleration, and this imbalance accelerates the fluid until the associated meridional component of the electromagnetic body force re-establishes a balance of forces. For the axial field, the largest inner core meridional circulation is $O(M^{-1})$, and is driven by: (i) the axial variation of the $O(1)$ u_θ through each Hartmann layer (Hartmann-layer pumping), and (ii) by the axial variation of the $O(M^{-1})$ u_θ in the inner core. For the non-uniform magnetic field, the variations of $u_{\theta i}$ drive an $O(1)$ meridional circulation, so that we can ignore the $O(M^{-1})$ Hartmann-layer pumping. The extension of the present analysis to determine the $O(M^{-1})$ meridional circulation is straightforward (Tolley 1991).

For a uniform axial magnetic field, there is no jump in the $O(1)$ pressure across the free shear layer at $r = a$, and the axial variation of $u_{\theta f}$ drives an $O(1)$ meridional circulation inside the free shear layer. For the non-uniform axisymmetric magnetic field, there is a jump in the $O(1)$ pressure across the free shear layer at $\Psi = \Psi_{ab}$, and the component of the centrifugal acceleration which is parallel to the local magnetic field drives an $O(M^{\frac{1}{2}})$ meridional circulation inside this layer. Using the stretched coordinate $\xi = M^{\frac{1}{2}}(\Psi - \Psi_{ab})$ in (23a), (23c), (24) and (26b), with the radial coordinate and magnetic field in the free shear layer given by (62), and the asymptotic expansion for $u_{\theta f}$ given by (61c), the appropriate asymptotic expansions in the free shear layer are

$$p_f = p_f^0 + M^{-\frac{1}{2}} p_f' + O(M^{-1}), \tag{79a}$$

$$u_{\Phi f} = M U_{\Phi f} + M^{\frac{1}{2}} \tilde{u}_{\Phi f} + O(1), \tag{79b}$$

$$u_{\Psi f} = M^{\frac{1}{2}} \tilde{u}_{\Psi f} + u_{\Psi f}^0 + O(M^{-\frac{1}{2}}). \tag{79c}$$

The leading-order equations are

$$\tilde{r} \frac{\partial p_f^0}{\partial \xi} = -\tilde{B} \tilde{u}_{\Psi f}, \tag{80a}$$

$$-\frac{1}{\tilde{r}} \frac{\partial \tilde{r}}{\partial \Phi} U_{\theta f}^2 = -\frac{\partial p_f^0}{\partial \Phi} + \tilde{r}^2 \tilde{B} \frac{\partial^2 U_{\Phi f}}{\partial \xi^2}, \tag{80b}$$

$$\frac{\tilde{r}}{\tilde{B}} \frac{\partial \tilde{u}_{\Psi f}}{\partial \xi} + \frac{\partial}{\partial \Phi} \left(\frac{U_{\Phi f}}{\tilde{B}} \right) = 0. \tag{80c}$$

The quantities $\tilde{r}$ and $\tilde{B}$ are given in (62) and are functions only of Φ. The $O(M^{\frac{1}{2}})$ velocity stream function in the free shear layer, $\tilde{G}_f$, is defined as

$$\tilde{u}_{\Psi f} = \frac{\tilde{B}}{\tilde{r}} \frac{\partial \tilde{G}_f}{\partial \Phi}, \quad U_{\Phi f} = -\tilde{B} \frac{\partial \tilde{G}_f}{\partial \xi}. \tag{81a, b}$$

Eliminating the pressure from (80) and using (81), the leading-order governing equation for the velocity stream function is

$$\tilde{r}^2 \tilde{B}^2 \frac{\partial^4 \tilde{G}_f}{\partial \xi^4} - \frac{\partial}{\partial \Phi} \left(\frac{\tilde{B}^2}{\tilde{r}^2} \frac{\partial \tilde{G}_f}{\partial \Phi} \right) = \frac{1}{\tilde{r}} \frac{\partial \tilde{r}}{\partial \Phi} \frac{\partial}{\partial \xi} (U_{\theta f}^2). \tag{82}$$

The boundary conditions which must be satisfied are

$$\tilde{G} \to 0, \quad \frac{\partial \tilde{G}_f}{\partial \xi} \to 0 \quad \text{as} \quad \xi \to \pm \infty, \tag{83a}$$

$$p_f^0 \to p_i(\Psi_{ab}, \Phi) \quad \text{as} \quad \xi \to -\infty, \quad p_f^0 \to p_o(\Psi_{ab}, \Phi) \quad \text{as} \quad \xi \to +\infty. \tag{83b}$$

The intersection regions at the crystal face and crucible bottom accommodate a simple exponential decrease of the velocity $\tilde{u}_{\Psi f}(\xi, \Phi_b)$, and the conditions on $U_{\Phi f}$ and the pressure are

$$U_{\Phi f}(\xi, \Phi_b) = U_{\Phi f}(\xi, \Phi_t) = 0 \quad \text{for all} \quad \xi, \tag{84a}$$

$$p_f^0(\xi, \Phi_b) \to p_i(\Psi_{ab}, \Phi_b), \quad p_f^0(\xi, \Phi_t) \to p_i(\Psi_{ab}, \Phi_t) \quad \text{for} \quad \xi < 0, \tag{84b, c}$$

$$p_f^0(\xi, \Phi_b) \to p_o(\Psi_{ab}, \Phi_b), \quad p_f^0(\xi, \Phi_t) \to p_o(\Psi_{ab}, \Phi_t) \quad \text{for} \quad \xi > 0. \tag{84d, e}$$

The governing equation (82) with the boundary conditions (83), (84) constitute a well-posed boundary value problem. As with the azimuthal velocity in the free shear layer, the governing equation involves variable coefficients and a numerical solution,

which treats the singularities at Φ_t and Φ_b, is necessary. The important features of the free shear layer for a non-uniform, axisymmetric magnetic field are: (i) that it involves a very strong $O(M^{\frac{1}{2}})$ internal meridional circulation, which provides vigorous local mixing and a barrier to heat and mass transfer between the core regions: and (ii) that it matches the jump in pressure (84) between the core regions.

5. Results for two simple shaped magnetic fields

In this section, we consider two field configurations corresponding to field case II. The first field configuration is the simplest non-uniform axisymmetric magnetic field that satisfies (2), (3), and has the dimensionless form

$$B_z(r,z) = -\left(\frac{z}{\alpha b}-1\right), \quad B_r(r,z) = \frac{r}{2\alpha b}, \tag{85a, b}$$

$$\Psi(r,z) = \frac{r^2}{2}\left(1-\frac{z}{\alpha b}\right), \quad \Phi(r,z) = z\left(1-\frac{z}{2\alpha b}\right)+\frac{r^2}{4\alpha b}. \tag{85c, d}$$

Here, b is the non-dimensional melt depth, and α is some constant. The value of α is taken to be greater than one, so that the axial magnetic field component is always positive, and there is no point where $\boldsymbol{B} = 0$. The smallest value of the magnetic field occurs at $r = 0$ and $z = b$, where the dimensional field strength is $B_0(1-1/\alpha)$. This minimum field strength must be greater than 0.2 T so that the inertialess approximation is valid everywhere. Figure 2(b) illustrates the magnetic field configuration for $\alpha = 1.4$.

Using (45a), (46a) and (85c), the functions $R(r)$ and $\rho(r,z)$ can be determined by finding the magnetic streamline which is at the radial coordinate r at $z = b$. Here,

$$\Psi(r,b) = \Psi_t = \frac{r^2}{2\alpha}(\alpha-1) \quad \text{for} \quad 0 \leqslant r \leqslant a, \tag{86a}$$

$$r = \left(\frac{2\alpha\Psi_t}{\alpha-1}\right)^{\frac{1}{2}} \quad \text{for} \quad 0 \leqslant \Psi_t \leqslant \Psi_{ab}, \tag{86b}$$

$$R(r) = r\left(\frac{\alpha-1}{\alpha}\right)^{\frac{1}{2}} = \left(2\Psi_t\right)^{\frac{1}{2}}, \tag{86c}$$

$$\rho(r,z) = r\left(\frac{b(\alpha-1)}{\alpha b-z}\right)^{\frac{1}{2}} = \left(\frac{2\alpha b\Psi_t}{\alpha b-z}\right)^{\frac{1}{2}}. \tag{86d}$$

Throughout this section, we will use Ψ_t to denote a particular magnetic streamline which intersects both the crystal face and the crucible.

The current stream function, h_s^1 is given by (56). With the magnetic field configuration (85) together with the coordinate values (86b, c), the boundary condition (55c) on the current stream function at $z = b$ determines the coefficients A_n, where

$$A_n = -\frac{2\gamma(\alpha-1)(1-\epsilon)a}{X_n(\gamma\alpha+(2\alpha-1)X_n)J_2(X_n)}. \tag{87}$$

Here, $\gamma = \delta MaB_z(r,b) = \delta Ma(\alpha-1)/\alpha$ is the ratio of the local electrical resistances and J_2 is the second-order Bessel function of the first kind. For the magnetic field configuration (85), the axial component of the magnetic field is constant at the crystal face, and γ is then constant for all r.
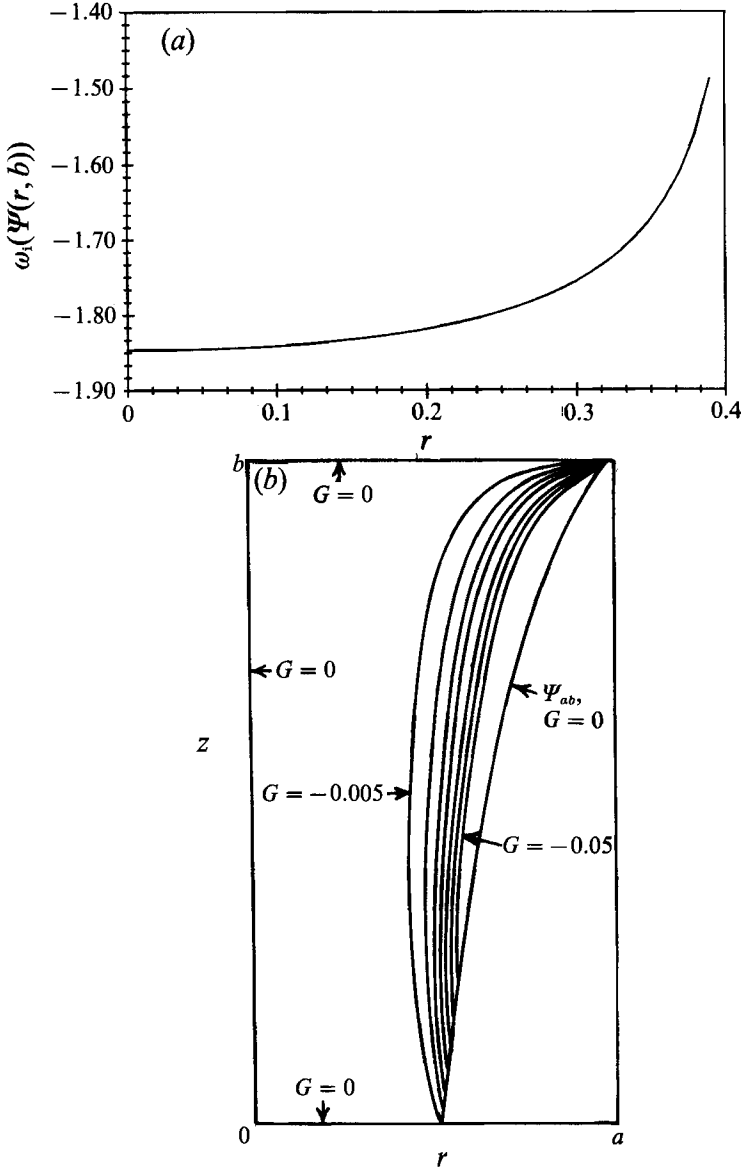
FIGURE 3. (a) Inner core angular velocity $\omega_i(\Psi)$ versus r at $z = b$ for the field configuration (85). Here $a = 0.4$, $b = 1.0$, $\alpha = 1.4$, $\epsilon = -2.0$ and $\gamma = 8.478$. (b) Inner core velocity streamlines, G, for field configuration (85), with $a = 0.4$, $b = 1.0$, $\alpha = 1.4$, $\epsilon -2.0$ and $\gamma = 8.478$. The circulation is clockwise with $G < 0$ for $0 < \rho < \rho(\Psi_{ab})$, with contour levels from -0.05 to 0 by 0.005.

The angular velocity $\omega_i(\Psi)$ is given by (60), and a plot of ω_i versus r at $z = b$ is presented in figure 3(a) for $a = 0.4$, $b = 1.0$, $\alpha = 1.4$, $\epsilon = -2.0$, $\gamma = 8.478$. For $R_c = 0.095$ m and $\alpha = 1.4$, $\gamma = 8.478$ corresponds to $B_0 = 0.7$ T, or an axial field strength of $B_0 B_z(r, b) = 0.2$ T at the crystal face. Near $r = a$, the value of $\omega_i(\Psi)$ asymptotically approaches the value of ω_i for $\gamma \ll 1$. For the magnetic field (85) with $\alpha = 1.4$, this value is $\omega_i = (\alpha(\epsilon + 1) - 1)/(2\alpha - 1) = -1.33$. Near $r = a$, the electric current density sees the Hartmann layer as the lower-resistance path, since the crystal edge has an infinitely small area, and an infinitely large resistance. Thus, near $r = a$, most of the

current is in the top Hartmann layer, so that $h_s^1(r, b)$ is tending toward zero, and ω_i is approaching -1.33. As r decreases from a, the fraction of current in the crystal increases, and ω_i tends toward a value of ϵ.

The behaviour of ω_i for other values of α, γ and ϵ is very similar to that of figure 3(a). In all cases, ω_i increases slowly from a value near ϵ at the crystal centre to a value approaching $\omega_i = (\alpha(\epsilon + 1) - 1)/(2\alpha - 1)$ as r or Ψ_t increases to a or Ψ_{ab}, with the largest change in ω_i taking place near the crystal edge.

The velocity stream function $G(\Psi, \Phi)$ given by (78a) can be evaluated along each streamline Ψ_t. To perform the integrations over the dummy variable Φ^*, we rewrite the variable dependence of Φ^* in terms of the radial and axial coordinates, while requiring that the integrand is evaluated along a fixed magnetic streamline, Ψ_t. Using (14), (46e), (85) and (86d),

$$d\Phi = B_r(\rho, z)\,d\rho + B_z(\rho, z)\,dz,$$

$$= \frac{\rho}{2\alpha b}\frac{\partial\rho}{\partial z}dz + \left(1 - \frac{z}{\alpha b}\right)dz = \left\{\frac{2(\alpha b - z)^3 + \alpha b\Psi_t}{2\alpha b(\alpha b - z)^2}\right\}dz. \tag{88}$$

With the notation of (75d, e), there are four integrals which must be evaluated, namely $f_1(\Psi_t, \Phi)$, $f_1(\Psi_t, \Phi_t)$, $f_2(\Psi_t, \Phi)$, and $f_2(\Psi_t, \Phi_t)$, with $\Phi_0 = \Phi_b$ denoting the value of Φ at which the magnetic streamline Ψ_t contacts the crucible bottom at $z = 0$, and Φ_t denoting the value of Φ at which the magnetic streamline Ψ_t contacts the crystal face at $z = b$. Using the field configuration (85), the radial coordinate along Ψ_t (86d), and the change of variables (88), the four integrals are evaluated in z, where

$$f_1(\Psi_t, z) = \Psi_t^2(\alpha b)^3\left\{\frac{1}{(\alpha b - z)^2} - \frac{1}{(\alpha b)^2}\right\}, \tag{89a}$$

$$f_2(\Psi_t, z) = 2\Psi_t(\alpha b)^2\left\{\frac{1}{(\alpha b - z)} - \frac{1}{\alpha b}\right\}. \tag{89b}$$

The values of f_1 and f_2 at Φ_t are given by (89) evaluated at $z = b$. The velocity stream function (78a) is

$$G(\Psi_t, \Phi) = G(\Psi_t, z)$$

$$= -\frac{d}{d\Psi}(\omega_i^2)(\alpha b)^3\Psi_t^2\left\{\frac{1}{(\alpha b - z)^2} - \frac{1}{(\alpha b)^2} - \left(\frac{\alpha b}{\alpha b - z} - 1\right)\left(\frac{1}{b^2(\alpha - 1)} - \frac{\alpha - 1}{(\alpha b)^2}\right)\right\}. \tag{90}$$

The velocity streamlines for $\alpha = 1.4$, $a = 0.4$, $b = 1.0$, $\gamma = 8.478$, and $\epsilon = -2.0$ are shown in figure 3(b). The circulation is clockwise, with the sign of G and the direction of circulation dependent on the sign of ω_i. For the field configuration (85), ω_i is always increasing with increasing Ψ. Thus, while ω_i may be positive or negative depending on the value of ϵ, the value of $d\omega_i/d\Psi$ is always positive. For corotation ($\epsilon > 0$) the direction of the circulation will be reversed, or counterclockwise, from that of counter-rotation ($\epsilon < 0$).

The primary circulation for the field configuration (85), and all values of ϵ, α, and γ, is a cell which closely follows the magnetic streamlines in the inner core, with flow either radially outward (clockwise circulation) or radially inward (counterclockwise circulation) near the crystal edge. The large circulation present near the crystal edge is due to the large change of ω_i which occurs over the outer half to one-quarter of the inner core. For counter-rotation, the inner core flow involves direct flow from the crucible bottom to the crystal face, with the magnitude of the flow increasing for

increasing r and directed almost tangent to the magnetic streamlines. The flow completes its circuit downward through the free shear layer near the magnetic streamline Ψ_{ab}. For corotation, the circulation is reversed or counterclockwise, and the flow travels up from the crucible bottom through the free shear layer, to the crystal edge. The flow circulation spreads radially inward and axially downward, with the velocity streamlines almost tangent to the magnetic streamlines in the inner core. The results for other values of α and γ are qualitatively similar. For any α and γ, the circulation direction changes with a change in sign of the differential rotation ϵ, and the magnitude of the circulation increases with increasing $|\epsilon|$.

The second configuration considered for the field case II is more complex than the magnetic field (85), and incorporates an axial field component which varies with r at $z = b$. The dimensionless magnetic field considered is of the form

$$B_z(r,z) = 1 + 2Kr^2 - 4Kz^2, \quad B_r(r,z) = 4Krz, \tag{91a, b}$$

$$\Psi(r,z) = \tfrac{1}{2}r^2 + \tfrac{1}{2}Kr^4 - 2Kr^2z^2, \quad \Phi(r,z) = z + 2Kr^2z - \tfrac{1}{3}4Kz^3, \tag{91c, d}$$

where K is a constant. The minimum dimensional field strength is $B_0(1 - 4Kb^2)$, which must be greater than or equal to 0.2 T. As no stagnation points in the magnetic field are allowed for field case II, the field (91) is restricted to having only a positive axial field component, so that $K > 1/4b^2$.

Using (45a), (46a), (91c), the functions $R(r)$ and $\rho(r,z)$ are found by determining the value of the magnetic streamline at (r, b). Here,

$$\Psi(r,b) = \Psi_t = \tfrac{1}{2}Kr^4 + Kg(b)r^2, \quad 0 \leqslant \Psi_t \leqslant \Psi_{ab}, \tag{92a}$$

$$r = \{-g(b) + (g(b)^2 + 2\Psi_t/K)^{\frac{1}{2}}\}^{\frac{1}{2}}, \tag{92b}$$

$$R = \{-g(0) + (g(0)^2 + 2\Psi_t/K)^{\frac{1}{2}}\}^{\frac{1}{2}}, \tag{92c}$$

$$\rho = \{-g(z) + (g(z)^2 + 2\Psi_t/K)^{\frac{1}{2}}\}^{\frac{1}{2}}, \tag{92d}$$

$$g(z) = (1 - 4Kz^2)/2K. \tag{92e}$$

The current stream function (56) can be determined using the boundary condition (55c), with the field configuration (91) and the coordinate values (92). The coefficients A_n are approximately

$$A_n = -\left(\frac{C_3 I_3 + C_4 I_4 + C_5 I_5}{a^2 C_1 J_2^2(X_n) + C_2 I_2}\right), \tag{93}$$

where

$$C_1 = K\delta Mg(0)\,g(b) + X_n\left(\frac{g(0) + g(b)}{2a}\right),$$

$$C_2 = 2K\delta Mg(0) + \frac{X_n}{a}, \quad I_2 = \int_0^a r^3 J_1^2\left(\frac{X_n r}{a}\right)\mathrm{d}r,$$

$$C_3 = 2K\delta Mg(b)^2(1-\epsilon), \quad C_4 = 3K\delta Mg(b)\,(1-\epsilon), \quad C_5 = K\delta M(1-\epsilon),$$

$$I_m = \int_0^a q_m(r)\,J_1\left(\frac{X_n r}{a}\right)\mathrm{d}r \quad \text{with} \quad q_3(r) = r^2, \quad q_4(r) = r^4, \quad q_5(r) = r^6.$$

The integrals I_m for $m = 3$, 4, 5 can be expressed analytically using recurrence relations for Bessel functions (Abramowitz & Stegun 1970), while the integral I_2 is evaluated numerically.

With the coefficients (93), the angular velocity $\omega_i(\Psi)$ can be determined for the magnetic field configuration (91). Figure 4(a–c) presents plots of ω_i for $\epsilon = 3.0$,
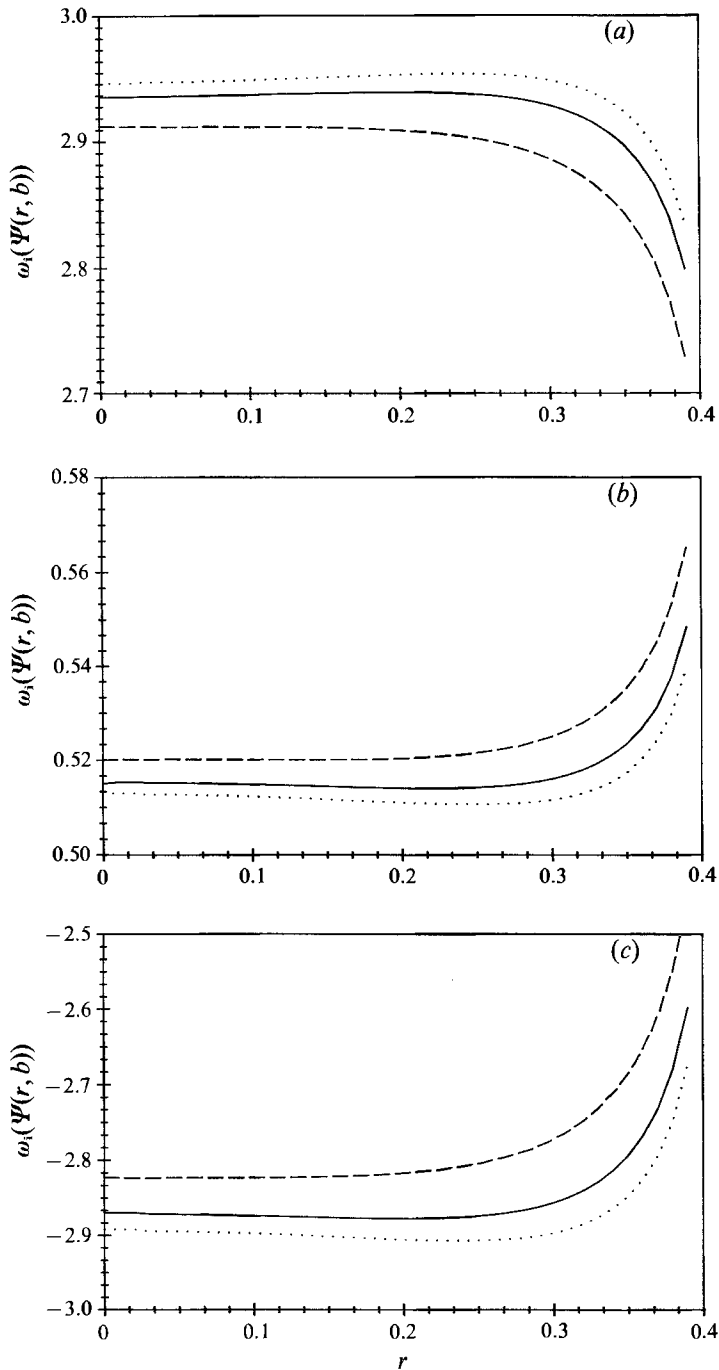
FIGURE 4. Inner core angular velocity $\omega_i(\Psi)$ versus r at $z = b$ for the field configuration (91), with $K = 0.2$ (----), 0.215 (——), 0.222 (......). The value of $M\delta$ for each K-value corresponds to a silicon melt with a 0.2 T field at the centre of the crystal face, with $b = 1.0$ and $a = 0.4$. (a) $\epsilon = 3.0$; (b) $\epsilon = 0.5$; (c) $\epsilon = -3.0$.
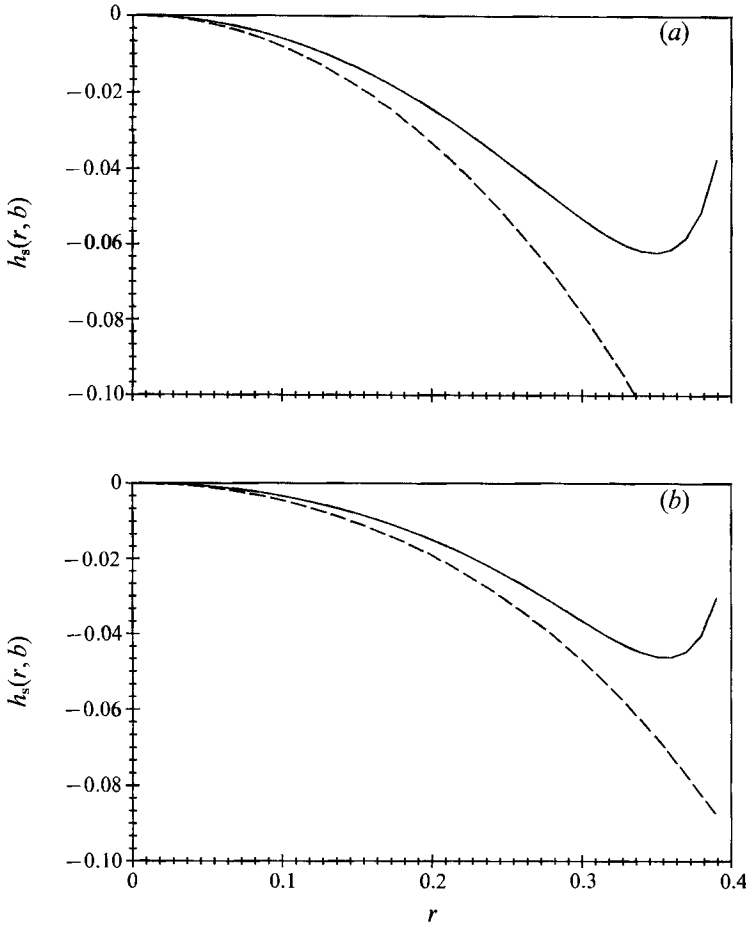
FIGURE 5. Crystal electric current stream function versus r at $z = b$, plotted with $(\epsilon - 1)R^2$ (-----) for field configuration (91), for $\epsilon = -3.0$ with (a) $K = 0.2$, and (b) $K = 0.222$.

0.5, and -3.0, respectively. On each plot the results for three magnetic field configurations corresponding to (91) with $K = 0.2, 0.215$, and 0.222, are shown with a non-dimensional melt depth $b = 1.0$. The value of $M\delta$ for each case corresponds to silicon with a 0.2 T field at the centre of the crystal face. For any axisymmetric field configuration, the angular velocity approaches a value corresponding to that for $\gamma \ll 1$ as $r \to a$. Near $r = 0$, the angular velocity approaches the value of ϵ. Examination of figure 4 (a–c) shows that over a large range of r, ω_i stays relatively constant, with a value near ϵ. The value of $\gamma(r)$ is less for lower K-values over the entire range in r, and the deviation from rotation with the crystal begins at a smaller value of r for $K = 0.2$ than for $K = 0.222$. This behaviour is evident in the plots of the crystal electric current stream function at $z = b$ for $\epsilon = -3.0$ and $K = 0.2, 0.222$ shown in figure 5 (a, b). These plots also include $(\epsilon - 1)R^2$, which is the value of the crystal electric current stream function for $\gamma \gg 1$. For $K = 0.2$, this current stream function deviates from $(\epsilon - 1)R^2$ by 30% at $r = 0.2$, but by 93% at $r = 0.3$. For $K = 0.222$, the deviation from $(\epsilon - 1)R^2$ is 25% at $r = 0.2$, and increases to 33% at $r = 0.3$.

The velocity stream function $G(\Phi, \Psi)$ given by (78a) can be evaluated in a manner similar to that for the first field case considered, although the integration of the
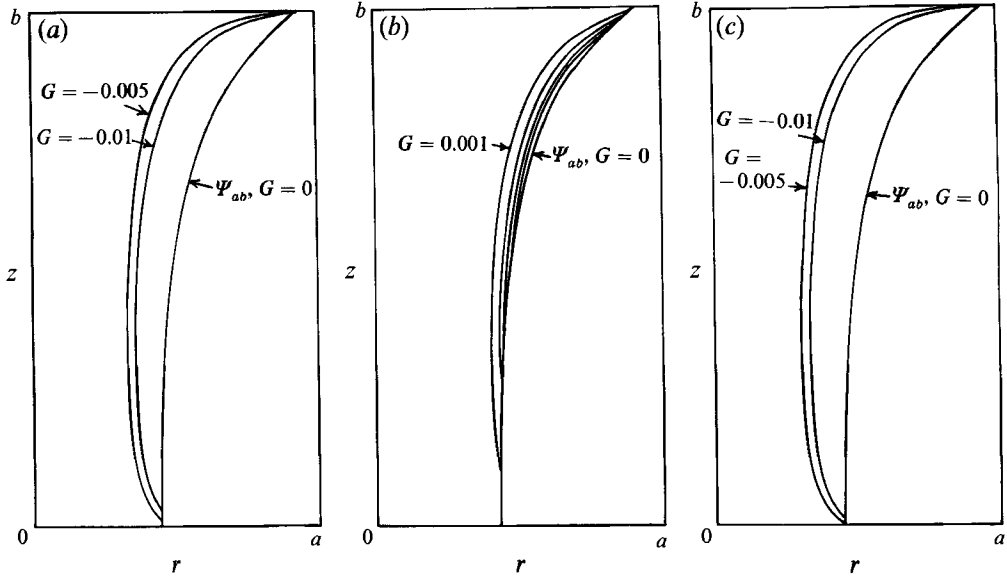
FIGURE 6. Inner core velocity streamlines, G, for field configuration (91) with $K = 0.2$, $B_0 = 1.0$ T, $a = 0.4$, $b = 1.0$ and $0 < \rho < \rho(\varPsi_{ab})$. (a) $\epsilon = 3.0$, circulation is clockwise, with contour levels from -0.01 to 0 by 0.005; (b) $\epsilon = 0.5$, circulation is counterclockwise, with contour levels 0 to 0.01 by 0.001; (c) $\epsilon = -3.0$, circulation is clockwise, with contour levels -0.01 to 0 by 0.005.

functions f_1 and f_2 must be done numerically. For the field case (91), the variable dependence on $\varPhi$ is rewritten so that the integration is along constant $\varPsi_t$. Using (46 e),

$$\mathrm{d}\varPhi = B_r(\rho, z)\frac{\partial\rho}{\partial z}\mathrm{d}z + B_z(\rho, z)\,\mathrm{d}z$$

$$= \frac{B^2}{B_z}\mathrm{d}z \text{ along constant } \varPsi_t. \tag{94}$$

With (94), the integrals (75 d,e) can be written as

$$f_1(\varPsi_t, z) = \int_0^z -\frac{\rho^4}{2B_z}\mathrm{d}z^* \text{ along } \varPsi_t \text{ constant,} \tag{95}$$

$$f_2(\varPsi_t, z) = \int_0^z \frac{\rho^2}{B_z}\mathrm{d}z^* \text{ along } \varPsi_t \text{ constant.} \tag{96}$$

The integrals $f_1(\varPsi_t, \varPhi_t)$ and $f_2(\varPsi_t, \varPhi_t)$ are the integrals of (95), (96) evaluated from $z = 0$ to $z = b$.

The velocity streamlines $G(\varPsi_t, z)$ are shown in figure 6 (a–c) for $\epsilon = 3.0$, 0.5, and -3.0, for the magnetic field configuration (91) with $K = 0.2$. The direction of the circulation is always clockwise for the rotation rates $\epsilon < 0$ and $\epsilon > 1$. This behaviour is controlled by the dependence of the velocity stream function on ω_i and $\mathrm{d}\omega_i/\mathrm{d}\varPsi$. As illustrated in figures 4 (a) and 4 (c), ω_i increases for counter-rotation, and decreases for corotation when $\epsilon > 1$. This means that the product of $\omega_i\,\mathrm{d}\omega_i/\mathrm{d}\varPsi$ is negative for $\epsilon < 0$ and $\epsilon > 1$. With $G(\varPsi, \varPhi)$ defined by (78a), the net sign of G for these two ranges of ϵ will yield $G < 0$, or clockwise circulation. The only possibility of counterclockwise circulation is for $0 \leqslant \epsilon < 1$, or small corotation, with the field configuration (91).

The changes in velocity stream function with increasing K, for a fixed value of $\epsilon < 0$ or $\epsilon > 1$, are: (i) a small increase in the dimensionless magnitude of the circulation; (ii) a compression of the circulation cell toward $\varPsi = \varPsi_{ab}$; and (iii) a shift of the $\varPsi_{ab}$ streamline toward the centreline. The increase in dimensionless circulation magnitude is a result of the increase in $d\omega_i/d\varPsi$ as K increases from 0.2 to 0.222. The compression of the circulation cell near the $\varPsi_{ab}$ magnetic streamline is a result of the relatively flat ω_1 profile. For increasing K-values, the angular velocity is almost constant for an increasing range of the magnetic streamlines contacting the crystal face. It is only near the outer one-third or one-quarter of the fieldlines contacting the crystal face that any significant deviation occurs from $\omega_i \sim \epsilon$ when $K = 0.215$ or 0.222. With the variation of ω_i concentrated at magnetic streamlines near the crystal edge, the meridional circulation will be concentrated along these same magnetic streamlines for $0 < z < b$. As K increases, the radial spread of the magnetic streamlines increases between $z = 0$ and $z = b$, and the magnetic field lines near the crystal edge move to a corresponding radial position which is closer to the centreline at $z = 0$. This results in a larger radial component of velocity near the crystal face, where the radial velocity is directed either radially outward (clockwise circulation) or inward (counterclockwise circulation). As $|\epsilon|$ is made larger, the dimensionless circulation magnitude increases slightly. This behaviour is simply related to the increase in $|\omega_i|$. For large differential rotation of the crystal, this will produce a larger radial component of flow near the crystal face.

6. Discussion

We have considered the isothermal rotationally driven flow in a model CZ crystal growth system with an applied non-uniform axisymmetric magnetic field. There are several characteristics of the isothermal flows driven by differential rotation in a CZ silicon crystal growth system which indicate the potential for improved crystal quality by using a shaped magnetic field. The analysis presented in this paper identifies two categories of non-uniform, axisymmetric fields, only one of which will produce the $O(1)$ meridional circulations driven by differential rotation.

Field case I is a field configuration for which there are no magnetic field lines which contact both the crystal and any crucible boundary. The inner core region is bounded by the centreline, crystal face, a portion of the free surface, and the dividing magnetic field line $\varPsi = 0$ which extends from $r = 0$ to a point on the free surface. The outer core region is bounded by the centreline, crucible boundaries, a portion of the free surface, and the dividing magnetic field line $\varPsi = 0$. The analysis shows that the inner and outer inviscid core regions are in rigid-body rotation with either the crystal rotation rate ϵ in the inner core, or crucible rotation rate of 1 in the outer core. The inviscid core solutions are given by (43), (44) and (66). For this field configuration, no $O(1)$ core or Hartmann-layer meridional flows are present. The only meridional flow is contained entirely within the free shear layer which separates the two inviscid core regions. The free shear layer analysis for field case I is equivalent to that presented for field case II in §§3 and 4. The leading-order volume flow, confined to the free shear layer, is $O(M^{\frac{1}{2}})$.

For field case II, when there are magnetic field lines which contact both the crystal and any portion of the crucible, there is an $O(1)$ meridional circulation in the inner core in the melt region bounded by the magnetic field through the crystal edge. The magnetic field and melt interaction requires that the electric current density be along magnetic field lines, and that the $O(1)$ angular velocity in the inner core region be

constant along magnetic field lines. It is only with this field case II configuration that the centrifugal acceleration is dependent on the magnetic field configuration. For the rigid-body rotations of field case I, the pressure gradients parallel and perpendicular to the magnetic field lines exactly balance the centrifugal acceleration, and no $O(1)$ Lorentz force is required for force balance in the inviscid core regions. For field case II, the pressure gradient parallel to magnetic field lines must balance the component of centrifugal acceleration parallel to the magnetic field lines. However, this restricts the pressure gradient perpendicular to the magnetic field lines, and this component of the pressure gradient cannot balance the centrifugal acceleration in this direction. This imbalance drives an $O(1)$ volume flow in the inviscid inner core region where magnetic field lines intersect solid boundaries which are rotating with different angular velocities. The associated $O(1)$ Lorentz force provides the balancing force. The inner core solutions are given by (38), (40), (60) and (78). The inviscid outer core region continues to have an azimuthal velocity described by a rigid-body rotation, with solutions (44) and (66).

The $O(1)$ meridional circulation is not present when the applied field is a uniform axial magnetic field, where the leading-order flow driven by differential rotation is $O(M^{-1})$. This type of field is a singular limit of the generalized axisymmetric field analysis presented in this paper. For the $O(1)$ azimuthal velocity which is a function only of r, the radial pressure gradient can exactly balance the radially directed centrifugal acceleration in the inviscid core regions. It is only at $O(M^{-1})$ that an axial variation of the centrifugal acceleration is present in the inviscid inner core, which cannot be balanced exactly by the radial pressure gradient.

Two case II field configurations are considered. The results for the first field, given by (85), show that $\omega_i(\Psi)$ is always increasing for increasing Ψ or, equivalently, for increasing r. The limiting values between which $\omega_i(\Psi)$ varies on a fixed magnetic streamline are ϵ near $\Psi = 0$ and $\omega_i = (\alpha(\epsilon+1)-1)/(2\alpha-1)$ when $\gamma \ll 1$, near $\Psi = \Psi_{ab}$. The limiting value for $\gamma \ll 1$, for the first field (85) is always greater than ϵ. This behaviour determines the direction of circulation for the $O(1)$ meridional flows given by (90). Since $\omega_i(\Psi)$ is increasing with increasing Ψ for every value of ϵ, the overall sign of $G(\Psi, \Phi)$ is positive for $\epsilon > 1$ and $1 > \epsilon \geqslant 0$, with counterclockwise circulation, and negative for $\epsilon < 0$ with clockwise circulation.

For the second field configuration, given by (91), the behaviour of $\omega_i(\Psi)$ again determines the overall sign of the velocity stream function. For $\epsilon < 0$, $\omega_i(\Psi)$ increases with increasing Ψ or r, and the velocity stream function is negative, with clockwise circulation. For $\epsilon > 1$, $\omega_i(\Psi)$ decreases with increasing Ψ, and the velocity stream function is negative, with clockwise circulation. It is only for the range of small differential rotations $0 \leqslant \epsilon < 1$ that the velocity stream function is positive with counterclockwise circulation, as $\omega_i(\Psi)$ is positive and increasing with increasing Ψ.

For both field configurations, the velocity stream function is almost tangent to the magnetic field lines in the inner core. Near the crystal face, for counterclockwise circulation, the flow exits the free shear layer and top Hartmann layer near Ψ_{ab}, and spreads radially inward and axially downward into the inner core. For clockwise circulation, the flow moves axially upward toward the crystal face, closely following magnetic streamlines, converging near the crystal face, and entering the free shear layer near the Ψ_{ab} magnetic streamline.

The presence of $O(1)$ circulations driven by differential rotation will affect both the heat and mass transfer in the inner core, the Hartmann layers on the crystal face and crucible bottom, and the free shear layer. For heat transfer, the convective heat transfer due to the $O(1)$ flows driven by the differential rotation can no longer be

ignored as small, as is the case for the axial field (Hjellming & Walker 1987). Even with the non-uniform axisymmetric field, the buoyancy-driven circulation will be counterclockwise, with hot fluid rising along the vertical crucible wall and falling under the crystal. The thermocapillary flows, driven by the variation of surface tension with temperature, are present only in the region bounded by the free surface. This flow also represents a counterclockwise circulation. For field case II configurations in which the magnetic field lines contact the crystal face and crucible bottom, this will be the region for which $\Psi > \Psi_{ab}$. The area under the crystal, where $\Psi < \Psi_{ab}$, will have convective heat and mass transfer due to the flows driven by buoyancy and differential rotation. The outer core region with $\Psi > \Psi_{ab}$, vertical wall layer, free surface and crucible bottom Hartmann layers will have convective heat and mass transfer due to the flows driven by thermocapillarity and buoyancy. These two regions of the melt will be separated by the free shear layer along the Ψ_{ab} magnetic field line.

In the region bounded by the centreline, crystal face, crucible bottom and the Ψ_{ab} magnetic field line, the $O(1)$ differential rotation driven circulation will either: (i) introduce a larger vertical temperature variation if the circulation is clockwise and opposing the buoyancy-driven flow, or (ii) introduce a larger radial temperature variation if the circulation is counterclockwise and reinforcing the buoyancy-driven flow.

The mass transport in this inner region is more difficult to assess. Since the diffusivities of most mass species in silicon are small, there is only convective mass transport within the inner core, and convective and diffusive mass transport in the crystal face diffusion boundary layer. The convective mass transport in the crystal face diffusion layer must provide sufficient circulation to produce a uniform radial concentration of dopants and impurities at the growth interface. In addition, as crystal growth proceeds and the melt depth is depleted, any depth dependence of the combined flow field driven by buoyancy and differential rotation must be taken into account. Such changes in the melt flow with time may adversely affect the axial variation of dopant and impurity levels in the growing crystal, as well as influence the radial distribution of dopants and impurities (Hjellming 1990; Hjellming & Walker 1988b).

Although the thermally driven flow problem has not been addressed in this paper, some conclusions may be drawn for the shaped field case by comparison to the axial field results of Hjellming & Walker (1987) and Hjellming (1990). For both a shaped field and an axial field, the thermally driven flows will be $O(1)$, with the buoyancy-driven flows having a characteristic velocity of

$$U_b = \rho_0 g \alpha \Delta T_0 / \sigma B_0^2.$$

Here, α is the coefficient of thermal expansion ($\alpha = 1.41 \times 10^{-4} \text{ K}^{-1}$), and ΔT_0 is a characteristic temperature difference (approximately 25–50 K).

The results for the axial field indicate that the non-dimensional inner core circulation driven by buoyancy is decreasing with increasing magnetic field strength as the melt becomes conduction dominated. The convective heat transfer provided by buoyancy in the inner core, and by buoyancy- and thermocapillary-driven flows in the outer core region, is strongest for low field strengths and large depths (Hjellming 1990). If the magnetic field magnitudes of the field configurations (85) and (91) are used, the melt will probably be conduction dominated if only the thermally driven flow is present. Using the dimensional magnitude of the buoyancy-driven circulation in a conduction-dominated melt yields an inner core buoyancy-

driven circulation which may be 10–20 times smaller than the $O(1)$ inner core circulation driven by differential rotation with the shaped field case II. It is then anticipated that the convective heat transfer in the inner core region provided by this new $O(1)$ circulation will dominate that provided by the buoyancy-driven circulation, even at large depths where the buoyancy-driven flows in the inner core region are maximum (Hjellming 1990). Similarly, the disparity in circulation magnitude between the buoyancy-driven flow and rotationally driven flow in the inner core region suggests that the rotationally driven flow will also dominate convective mass transfer throughout the inner core and surrounding viscous layers. However, since the entire flow field will be a superposition of the two flows, both the direction and magnitude of the total flow field will be important.

It should also be noted that the depth dependence of the rotationally driven flows is confined to any depth dependence of the field configuration, as indicated by (78 a). One advantage of the shaped field is the ability to change the field configuration during the entire growth process, not just in magnitude but also in direction. This flexibility is available only with the field magnitude when uniform transverse or axial magnetic fields are used. Since it appears that the $O(1)$ rotationally driven circulation closely parallels the magnetic field lines, tailoring the flow throughout the growth process with changes in the field configuration is possible.

With the shaped magnetic field there is a substantial increase in the inner core circulation, the ability to tailor the rotationally driven flows along magnetic field lines at every melt depth, and vary the direction of this circulation, as the direction of the circulation is determined by the ratio of the angular velocity of the crystal to that of the crucible and magnetic field configuration through the relationships (60), (94). These features may introduce the mechanism for control of the heat and mass transport to the growth interface lacking in the uniform axial and transverse magnetic fields.

While the free shear solutions for the azimuthal and meridional problem are not presented, the free shear layer position and structure will play an important role in the mass transfer of oxygen and other impurities introduced through the ablation of the crucible. The leading-order circulation due to the variation of the centrifugal acceleration within the free shear layer is $O(M^{\frac{1}{2}})$, with this flow entirely contained within the free shear layer. From the axial field analysis of Hjellming & Walker (1987), the leading-order circulation within the free shear layer produced by the presence of thermocapillary flows is $O(1)$, with an $O(M^{\frac{1}{2}})$ axial velocity within the $O(M^{-\frac{1}{2}})$ free shear layer. This order of magnitude will hold for the shaped field as well. Since the free shear layer circulation due to the differential rotation is $O(M^{\frac{1}{3}})$ larger than that for thermocapillarity, one possible effect of this order of magnitude difference may be the blockage of oxygen-depleted fluid carried by thermocapillary flow along the free surface toward the crystal edge. In addition, given the direction of the rotationally driven flows, supplemental oxygen may be carried toward the crystal edge from the crucible bottom, creating a large concentration variation across and within the free shear layer.

For some field configurations, the thermocapillary flow will not be as strongly suppressed as it is with a uniform axial field, if the radial component of the shaped magnetic field is significant at the free surface, and the axial field component is reduced. This may result in an increased evaporation of oxygen carried by a larger volume of fluid travelling near the free surface, thus decreasing the overall oxygen level in the melt volume.

Also of interest with respect to the free shear layer and inner core circulations,

particularly for the two field cases (85) and (91) considered, is the decrease in the surface area exposed to direct flow from the crucible bottom to the crystal face. Since a magnetic field which spreads radially as z increases has a dividing magnetic streamline Ψ_{ab} which contacts the crucible bottom at $R(\Psi_{ab}) < a$, where a is the non-dimensional crystal radius, the vigorous free shear layer flows and bottom Hartmann layer flow have a reduced contact surface area at the crucible bottom, compared to a magnetic field which converges radially as z increases, with $R(\Psi_{ab}) > a$. This factor may be important in the transfer of oxygen directly from the crucible bottom to the crystal face (Tolley 1991).

If one considers a field configuration such as that used by Hirata & Hoshikawa (1989), there will be two free shear layers, one along the stagnation streamline $\Psi = 0$ from the centreline to $r = 1$, and another along the dividing streamline Ψ_{ab} which contacts the crystal face and the vertical crucible wall above the $\Psi = 0$ line and below the point $r = 1$ and $z = b$. This configuration will isolate the inner core region from the crucible bottom and free surface. With the large radial field component at the free surface, the thermocapillary flows are not highly suppressed, and the free shear layer along Ψ_{ab} will provide a barrier to direct convective mass transfer of oxygen-poor fluid to the crystal edge. However, there is probably direct flow along the magnetic streamlines from the vertical crucible wall to the crystal face, with the $O(M^{-1})$ Hartmann layer now on the vertical wall at $r = 1$.

REFERENCES

ABRAMOWITZ, M. & STEGUN, 1. A. 1970 *Handbook of Mathematical Functions.* Dover.

HICKS, T. W., ORGAN, A. E. & RILEY, N. 1989 Oxygen transport in magnetic Czochralski growth of silicon with a non-uniform magnetic field. *J. Cryst. Growth* **94**, 213–228.

HICKS, T. W. & RILEY, N. 1989 Boundary layers in magnetic Czochralski crystal growth. *J. Cryst. Growth* **96**, 957–968.

HIRATA, H. & HOSHIKAWA, K. 1989 Silicon crystal growth in a cusp magnetic field. *J. Cryst. Growth* **96**, 747–755.

HJELLMING, L. N. 1990 A thermal model for Czochralski silicon crystal growth with an axial magnetic field. *J. Cryst. Growth* **104**, 327–344.

HJELLMING, L. N. & WALKER, J. S. 1986 Melt motion in a Czochralski crystal puller with an axial magnetic field: isothermal motion. *J. Fluid Mech.* **164**, 237–273 (referred to herein as HWI).

HJELLMING, L. N. & WALKER, J. S. 1987 Melt motion in a Czochralski crystal puller with an axial magnetic field: motion due to buoyancy and thermocapillarity. *J. Fluid Mech.* **182**, 335–368.

HJELLMING, L. N. & WALKER, J. S. 1988*a* Melt motion in a Czochralski crystal puller with an axial magnetic field: uncertainty in the thermal constants. *J. Cryst. Growth* **87**, 18–32.

HJELLMING, L. N. & WALKER, J. S. 1988*b* Mass transport in a Czochralski crystal puller with an axial magnetic field: melt motion due to crystal growth and buoyancy. *J. Cryst. Growth* **92**, 371–389.

KURODA, E., KOZUKA, H. & TAKANO, Y. 1984 The effect of temperature oscillations at the growth interface on crystal perfection. *J. Cryst. Growth* **68**, 613–623.

LANGLOIS, W. E. 1984 Computer simulation of Czochralski melt convection in a magnetic field. *J. Cryst. Growth* **70**, 73–77.

LANGLOIS, W. E., HJELLMING, L. N. & WALKER, J. S. 1987 Effects of finite electrical conductivity of the crystal on hydromagnetic Czochralski flow. *J. Cryst. Growth* **83**, 51–61.

LANGLOIS, W. E., KIM, K. M. & WALKER, J. S. 1992 Hydromagnetic crystal growth. *J. Cryst. Growth* (to appear).

MORSE, P. M. & FESHBACK, H. 1953 *Methods in Theoretical Physics: Part* I. McGraw-Hill.

RAVISHANKAR, P. S., BRAGGINS, T. T. & THOMAS, R. N. 1990 Impurities in commercial-scale magnetic Czochralski silicon: axial versus transverse fields. *J. Cryst. Growth* **104**, 617–628.

THOMAS, R. N., HOBGOOD, H. M., RAVISHANKAR, P. S. & BRAGGINS, T. T. 1990 Melt growth of large diameter semiconductors: part II. *Solid State Technol.* **33**, 163–167.

TOLLEY, P. A. 1991 The use of non-uniform axisymmetric magnetic fields in silicon crystal growth. M.S.M.E. Dissertation, Department of Mechanical Engineering and Engineering Science, University of North Carolina at Charlotte, Charlotte, NC.

WILLIAMS, M. G. 1989 Melt flow in a Czochralski crystal puller with a transverse magnetic field. Ph.D. dissertation, Department of Theoretical and Applied Mechanics, University of Illinois at Urbana-Champaign, Urbana, IL.

WILLIAMS, M. G., WALKER, J. S. & LANGLOIS, W. E. 1990 Melt motion in a Czochralski crystal puller with a weak transverse magnetic field. *J. Cryst. Growth* **100**, 233–253.